

# NAVAL POSTGRADUATE SCHOOL MONTEREY, CALIFORNIA



## THESIS

### RADIATION PATTERN CALCULATION FOR MISSILE RADOMES IN THE NEAR FIELD OF AN ANTENNA

by

Scott M. Herzog

September 1996

Thesis Advisor:  
Second Reader:

David C. Jenn  
Robert E. Ball

19970129 048

Approved for public release; distribution is unlimited.

DTIC QUALITY INSPECTED 6

REPORT DOCUMENTATION PAGE			Form Approved OMB No. 0704-0188	
Public reporting burden for this collection of information is estimated to average 1 hour per response, including the time for reviewing instruction, searching existing data sources, gathering and maintaining the data needed, and completing and reviewing the collection of information. Send comments regarding this burden estimate or any other aspect of this collection of information, including suggestions for reducing this burden, to Washington Headquarters Services, Directorate for Information Operations and Reports, 1215 Jefferson Davis Highway, Suite 1204, Arlington, VA 22202-4302, and to the Office of Management and Budget, Paperwork Reduction Project (0704-0188) Washington DC 20503.				
1. AGENCY USE ONLY (Leave blank)	2. REPORT DATE September 1996	3. REPORT TYPE AND DATES COVERED Master's Thesis		
4. TITLE AND SUBTITLE RADIATION PATTERN CALCULATION FOR MISSILE RADOMES IN THE NEAR FIELD OF AN ANTENNA		5. FUNDING NUMBERS		
6. AUTHOR(S) Scott M. Herzog		8. PERFORMING ORGANIZATION REPORT NUMBER		
7. PERFORMING ORGANIZATION NAME(S) AND ADDRESS(ES) Naval Postgraduate School Monterey CA 93943-5000		10. SPONSORING/MONITORING AGENCY REPORT NUMBER		
9. SPONSORING/MONITORING AGENCY NAME(S) AND ADDRESS(ES)		11. SUPPLEMENTARY NOTES The views expressed in this thesis are those of the author and do not reflect the official policy or position of the Department of Defense or the U.S. Government.		
12a. DISTRIBUTION/AVAILABILITY STATEMENT Approved for public release; distribution is unlimited.		12b. DISTRIBUTION CODE		
13. ABSTRACT (maximum 200 words) An analytical model and computer simulation are presented for a radome located in the near field of an antenna. Using the computer code described here, design tradeoffs can be performed between electrical, structural, and aerodynamic properties of the radome. The code is based on a method of moments solution to the E-field integral equation for bodies of arbitrary shape. Measured radiation patterns for AGM-88 High Speed Antiradiation Missile (HARM) and AIM-9C missile radomes are compared to computed data.				
14. SUBJECT TERMS Radome, Method of Moments, PATCH.		15. NUMBER OF PAGES 83		
17. SECURITY CLASSIFICATION OF REPORT Unclassified		18. SECURITY CLASSIFICATION OF THIS PAGE Unclassified	19. SECURITY CLASSIFICATION OF ABSTRACT Unclassified	20. LIMITATION OF ABSTRACT UL
16. PRICE CODE				

NSN 7540-01-280-5500

Standard Form 298 (Rev. 2-89)  
Prescribed by ANSI Std. Z39-18 298-102



Approved for public release; distribution is unlimited.

**RADIATION PATTERN CALCULATION FOR MISSILE RADOMES  
IN THE NEAR FIELD OF AN ANTENNA**

Scott M. Herzog  
Lieutenant, United States Navy  
B.S.A.A.E., The Ohio State University, 1988

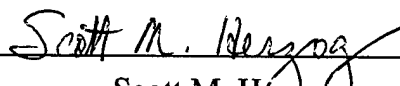
Submitted in partial fulfillment  
of the requirements for the degree of

**MASTER OF SCIENCE IN AERONAUTICAL ENGINEERING  
(AVIONICS)**

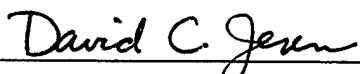
from the


**NAVAL POSTGRADUATE SCHOOL  
September 1996**

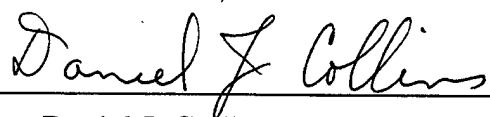
Author:

  
\_\_\_\_\_  
Scott M. Herzog

Approved by:

  
\_\_\_\_\_  
David C. Jenn, Thesis Advisor

  
\_\_\_\_\_  
Robert E. Ball, Second Reader

  
\_\_\_\_\_  
Daniel J. Collins, Chairman  
Department of Aeronautics & Astronautics



## **ABSTRACT**

An analytical model and computer simulation are presented for a radome located in the near field of an antenna. Using the computer code described here, design tradeoffs can be performed between electrical, structural, and aerodynamic properties of the radome. The code is based on a method of moments solution to the E-field integral equation for bodies of arbitrary shape. Measured radiation patterns for AGM-88 High Speed Antiradiation Missile (HARM) and AIM-9C missile radomes are compared to computed data.

## ACKNOWLEDGMENTS

I would like to thank Professor David C. Jenn for his guidance and assistance in undertaking this thesis. His expertise in radar and electromagnetics is truly an asset to the Naval Postgraduate School.

Many thanks to Colin Cooper of the ECE Computing Staff for his high degree of professionalism and assistance with the Suns workstations.

Most importantly I owe much gratitude to my wife and daughter, Holly and Rachel. Without your infinite patience, support, and advice I would not have been able to complete this project.

## TABLE OF CONTENTS

I. INTRODUCTION .....	1
II. ANALYSIS METHODS AND COMPUTER CODES .....	5
A. METHOD OF MOMENTS .....	5
B. RADOME WALL MODEL AND IMPEDANCE CALCULATION ....	9
C. PATCH AND RELATED PROGRAMS .....	15
D. RADOME PROGRAM .....	20
III. COMPUTER CODE VALIDATION .....	21
A. APERTURE MODEL .....	21
1. Patch Code Antenna Model .....	22
2. Radome Code Antenna Model .....	29
B. SCATTERING DISK TEST CASE .....	29
IV. DATA ANALYSIS .....	37
A. ANECHOIC CHAMBER FACILITY .....	37
B. PHASE CENTER FOR MICROLINE 56X1 HORN .....	38
C. AGM-88 HARM RADOME .....	41
D. AIM-9C RADOME .....	47



V. CONCLUSION .....	53
APPENDIX A. PROGRAM LISTING FOR IMPEDANCE CALCULATION .....	59
APPENDIX B. SAMPLE INPATCH FILE LISTING .....	61
APPENDIX C. PROGRAM LISTING FOR VOLTAGE TAPERING .....	65
APPENDIX D. PROGRAM LISTING FOR GEOMETRY COMBINING .....	67
LIST OF REFERENCES .....	69
INITIAL DISTRIBUTION LIST .....	71

## LIST OF FIGURES

<b>Figure 1.1</b>	Ray tracing .....	2
<b>Figure 1.2</b>	Spherical coordinate system .....	4
<b>Figure 2.1</b>	Geometry for EFIE .....	5
<b>Figure 2.2</b>	Stepped impedance transformer .....	9
<b>Figure 2.3</b>	Multi-layered radome wall geometry .....	11
<b>Figure 2.4</b>	HARM radome wall .....	13
<b>Figure 2.5</b>	AIM-9C radome wall .....	13
<b>Figure 2.6</b>	HARM radome impedance as a function of incidence angle .....	14
<b>Figure 2.7</b>	Relationships between PATCH and its pre- and post-processing programs .....	17
<b>Figure 2.8</b>	Plate composed of triangular facets .....	18
<b>Figure 3.1</b>	Microline 56X1 standard gain horn .....	21
<b>Figure 3.2</b>	Aperture model for Microline 56X1 antenna .....	23
<b>Figure 3.3</b>	Cosine on a pedestal .....	24
<b>Figure 3.4</b>	Effect of tapering .....	26
<b>Figure 3.5</b>	Effect of quadratic phase error .....	26
<b>Figure 3.6</b>	Comparison of main beam E-plane patterns .....	28
<b>Figure 3.7</b>	Comparison of main beam H-plane patterns .....	28
<b>Figure 3.8</b>	PEC disk in front of aperture .....	30

<b>Figure 3.9</b>	Patterns with aperture and disk .....	32
<b>Figure 3.10</b>	Effect of antenna surface impedance on the aperture pattern .....	33
<b>Figure 3.11</b>	Effect of antenna surface impedance on the aperture and disk pattern ..	34
<b>Figure 4.1</b>	HP X890A microwave horn .....	37
<b>Figure 4.2</b>	Anechoic chamber facility .....	39
<b>Figure 4.3</b>	Phase center adjustment .....	40
<b>Figure 4.4</b>	HARM (upper) and AIM-9C (lower) radomes in anechoic chamber ....	41
<b>Figure 4.5</b>	HARM radome model .....	42
<b>Figure 4.6</b>	Effect of varying aperture impedance .....	44
<b>Figure 4.7</b>	Effect of varying radome impedance .....	45
<b>Figure 4.8</b>	Comparison of measured and computed patterns for HARM radome ....	46
<b>Figure 4.9</b>	AIM-9C radome model .....	48
<b>Figure 4.10</b>	Effect of varying aperture impedance .....	49
<b>Figure 4.11</b>	Effect of varying radome impedance .....	50
<b>Figure 4.12</b>	Comparison of measured and calculated patterns for AIM-9C radome ..	51
<b>Figure 5.1</b>	Effect of HARM radome on antenna pattern .....	57
<b>Figure 5.2</b>	Effect of AIM-9C radome on antenna pattern .....	58

## I. INTRODUCTION

The radome is an essential part of communications and radar systems deployed on aircraft. It provides environmental protection for the antenna and therefore must withstand extreme aerodynamic and thermal stresses (such as on a supersonic missile) and must also effectively transmit electromagnetic radiation. For example, the radome is a critical component on an anti-radiation missile (ARM). An ARM uses a passive antenna to home in on enemy radar emissions. The emitted energy passes through the missile's radome, which has some loss and also introduces beam pointing error. The main beam's field of view (FOV) must be narrow enough for proper target discrimination, but wide enough for off-boresight intercept. The radome can also increase side lobe levels, which must remain low enough to prevent azimuth and elevation errors. The result is degraded antenna performance when the radome is present relative to when the antenna is operating isolated in free space.

Traditionally, aerodynamic, structural, and thermal requirements have dictated the design of a radome, with the electrical performance taken as a consequence. The analytical model and computer code described in this thesis can be used to optimize the overall design of the radome since electrical design tradeoffs can be performed concurrently with the aerodynamic and structural engineering. Therefore, an accurate analytical model of the antenna and radome is required for efficient, cost-effective radome design.

There are basically two methods of analyzing radomes of arbitrary shape: (1) ray tracing (geometrical optics), and (2) the method of moments (MM). For ray tracing, a spherical wave is assumed radiated from the antenna, which is approximately planar at the

radome so that the Fresnel reflection coefficients can be used. Rays are traced from the antenna to the radome surface, where reflections and refractions occur. The transmitted rays are used to reconstruct an aperture distribution. The far field is computed using radiation integrals [Ref. 1].

Ray tracing is only applicable for electrically large radomes that are in the far field of the antenna. For low side lobe antennas, multiple reflections are important, and a significant amount of bookkeeping is required to determine the ray trajectories. An example of ray tracing is illustrated in Figure 1.1.

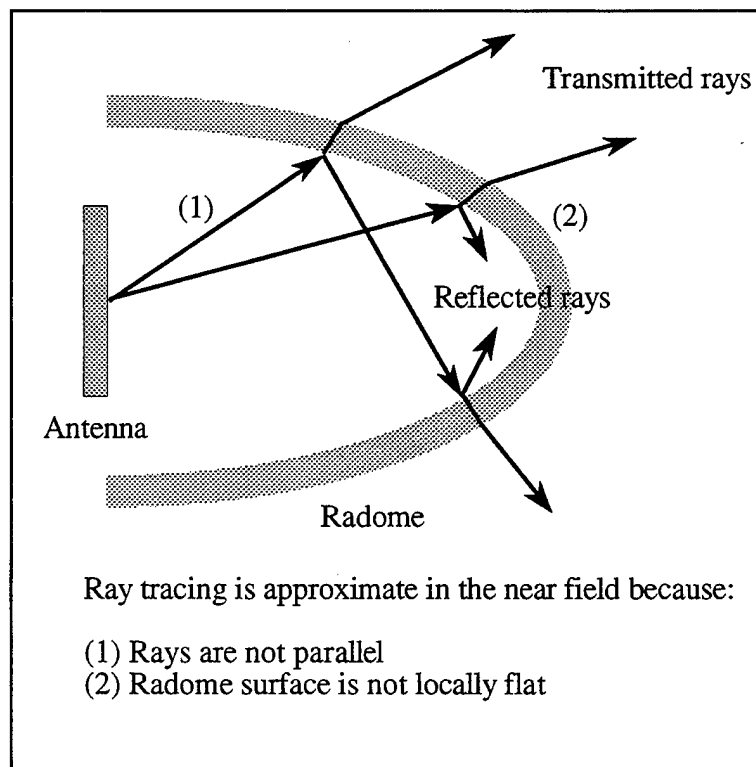


**Figure 1.1** Ray tracing

The computer code presented here uses a method of moments solution to the electric field integral equation to calculate the effect of a dielectric radome shell in the near field of an antenna. The method of moments is rigorous in that all multiple reflections between the radome walls are included. As will be demonstrated, the code is flexible as well as accurate and handles radomes of any shape and size (with size limited only by the available computer memory).

Chapter II reviews the analysis methods and computer codes. An overview of the method of moments is presented. Essentially the electric field integral equation is reduced to a matrix problem which is readily solved by numerical methods. Also, the equivalent single-layer impedance is derived for multiple layer radome walls. The impedance is calculated for two test radomes: an AGM-88 HARM and an AIM-9C. The impedance values are used by the method of moments computer codes. Chapter II concludes with a discussion of these codes. RADOME, a code developed by Francis [Ref. 2] and later improved by Klopp [Ref. 3], is limited to bodies of revolution (BOR), and uses a thin-shell approximation for the radome wall. In this thesis, a code developed by Sandia National Laboratories called PATCH [Ref. 4] is applied to the radome problem. It represents the radome as a collection of triangular patches which allows for virtually any geometry as well as various dielectric materials. Cartesian coordinates describe antenna and radome geometry in PATCH, while spherical coordinates describe the electromagnetic field. The coordinate systems are shown in Figure 1.2. Typically the radome is oriented with the axis of symmetry coincident with the  $z$ -axis.

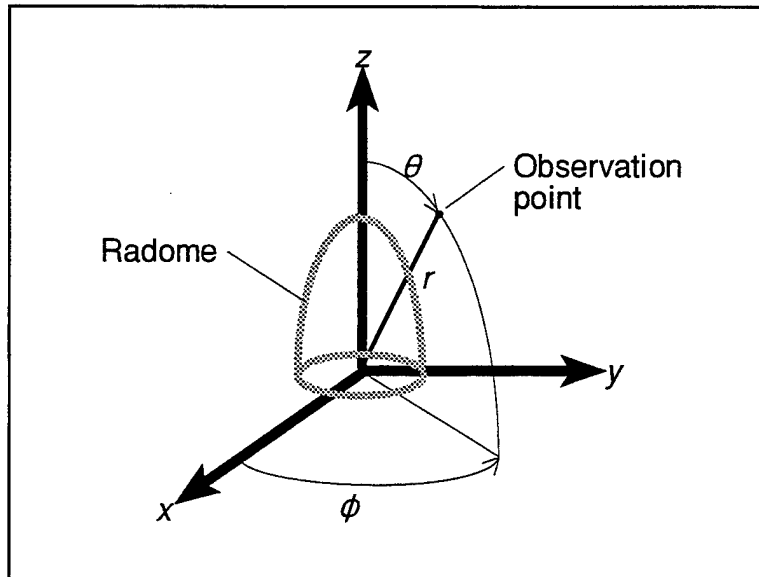


**Figure 1.2** Spherical coordinate system

Chapter III explains the procedure used to modify and validate PATCH. An antenna aperture model is developed for a standard gain horn that is used for both PATCH and RADOME programs. A test case was run and the computed results from both programs are compared to measured data obtained in the anechoic chamber. An additional test case is used to demonstrate the capability of PATCH to accurately calculate multiple reflections.

Chapter IV presents the data obtained by analyzing the two test radomes. The anechoic chamber facility is described and measuring techniques are discussed. Several improvements have been made since the chamber's inception. Automated measurements are made using a HP-8510 network analyzer linked to a personal computer.

Finally, Chapter V presents a summary of results and conclusions based on working with the code as a radome analysis tool. Sources of measurement error are discussed and recommendations are made to enhance the existing computer models and codes.

## II. ANALYSIS METHODS AND COMPUTER CODES

### A. METHOD OF MOMENTS

The computer codes that will be discussed in the following sections use the method of moments (MM) to calculate radome effects. A detailed discussion of this method can be found in [Ref. 1]. Only an overview of the method is presented here.

The electric field integral equation (EFIE) is commonly encountered in electromagnetics. This equation relates the scattered electric field to the electric current on the surface of an object. The EFIE is classified mathematically as a Fredholm equation since the limits of integration are fixed (i.e., over the body). Because the unknown variable appears only in the integrand, it is a Fredholm equation of the first kind.

To derive the EFIE, we first define the coordinate system shown in Figure 2.1. The target, or scattering body, is assumed (temporarily) to be a perfect electric conductor (PEC).

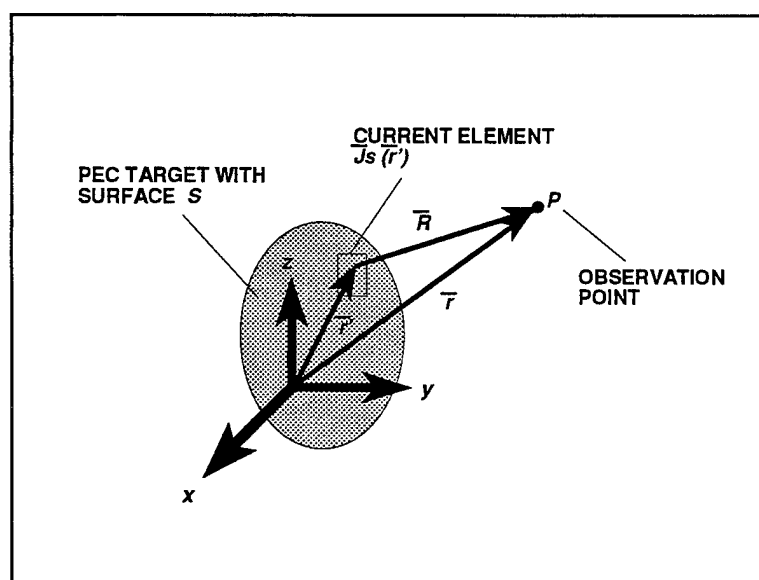


Figure 2.1 Geometry for EFIE



We will introduce a correction term later that will remove the PEC restriction. Note that in general,  $S$  includes both the radome and antenna surfaces. We define

$$R = |\bar{r} - \bar{r}'| = \sqrt{(x - x')^2 + (y - y')^2 + (z - z')^2} \quad (2.1)$$

and the free-space Green's function as

$$G(\bar{r}, \bar{r}') = \frac{e^{-jkR}}{4\pi R} \quad (2.2)$$

After some manipulation [Ref. 1, pp. 117-118], the final form of the EFIE suitable for solution by a numerical technique is

$$\bar{E}_i|_{tan} = \iint_S \left\{ j\omega\mu \bar{J}_s(\bar{r}') G(\bar{r}, \bar{r}') - \frac{j}{\omega\epsilon} [\nabla' \cdot \bar{J}_s(\bar{r}')] \nabla' G(\bar{r}, \bar{r}') \right\}_{tan} ds' \quad (2.3)$$

where  $\bar{E}_i$  is the incident electric field,  $\bar{J}_s$  is the surface current density,  $\mu$  is the permeability,  $\epsilon$  is the dielectric constant, and  $\omega$  is the angular frequency. Since the total electric field is the sum of the incident and scattered electric fields, by imposing the PEC boundary condition (total tangential electric field is zero), Equation 2.3 states that the tangential component of  $\bar{E}_i$  equals the tangential component of the scattered field.

This form of the equation can be applied to any arbitrary surface. The incident field is always known, and the surface current density is the only unknown. The incident field can be a plane wave or an impressed voltage on the surface of the body. Potentials on the antenna surfaces produce an electric field which then becomes the incident field on a scattering body

such as a radome. This interaction between the antenna and radome is embedded in Equation 2.3.

The method of moments is a procedure used to reduce the integral equation to a matrix problem. We start by representing the current in Equation 2.3 as a series with unknown expansion coefficients,  $I_n$ .

$$\bar{J}_s = \sum_{n=1}^N I_n \bar{J}_n \quad (2.4)$$

The vectors  $\bar{J}_n$  are known as the basis functions. These are either subsectional or entire domain functions, and are chosen to be accurate representations of the current and mathematically convenient (easy to integrate and differentiate). Typical subdomain basis functions include impulse functions, rectangular pulses, and overlapping triangular pulses. Entire domain functions include sinusoids and exponentials. A testing procedure is performed in which both sides of Equation 2.3 are multiplied by each testing function and integrated over its domain. Thus  $N$  equations are obtained, each with  $N$  terms. The simultaneous set of equations can be cast into matrix form and when solved yield

$$\mathbf{I} = \mathbf{Z}^{-1} \mathbf{V} \quad (2.5)$$

where  $\mathbf{I}$  is the vector containing the expansion coefficients,  $I_n$ .  $\mathbf{Z}$  is an impedance matrix and  $\mathbf{V}$  the excitation vector. Generally both of these have complex elements. The specific form of the elements depends on the choice of basis functions. The coefficients from Equation 2.5

are then used in Equation 2.4, which yields the surface current,  $\bar{J}_s$ . This in turn is used in the radiation integrals to find the fields due to the surface current.

The  $m^{\text{th}}$  element of the excitation vector  $\mathbf{V}$  in Equation 2.5 has the form

$$V_m = \iint_{S_m} \bar{E}_i \cdot \bar{J}_m^* ds \quad (2.6)$$

where  $\bar{J}_m^*$  is the testing function and  $\bar{E}_i$  the incident antenna field.  $S_m$  denotes the portion of the radome surface over which  $\bar{J}_m^*$  is nonzero. In general, the  $S_m$  can lie in the near field of the antenna and therefore no far field approximations can be applied. The antenna models in PATCH and RADOME differ, and both will be described later. Neither code has restrictions on the location of the radome relative to the antenna.

Equation 2.3 applies to a perfectly conducting surface. For thin dielectric shells such as radomes, the EFIE for perfect conductors is modified by adding a load term outside of the brackets [Ref. 1, p. 158]. This thin-shell approximation replaces the volume polarization currents flowing throughout the dielectric with a thin sheet of surface current. The result is that the elements of  $\mathbf{Z}$  in Equation 2.5 are also modified by the addition of a load term.

Overall, the method of moments provides a rigorous solution for the induced current density on a body. When properly applied, the series representation for the current will converge to the actual current as the number of basis functions is increased [Ref. 1]. Since the solution reduces to a matrix problem, MM is well-suited for computer coding.

Two MM solutions have been applied to the radome problem in this thesis. One solution (RADOME) applies only to bodies of revolution. By exploiting the rotational

symmetry of bodies such as ogives and hemispheres, basis functions can be chosen that reduce the number of linear equations that must be solved. The second solution (PATCH) uses triangular subdomains, which are the most flexible for modeling arbitrary surfaces.

## B. RADOME WALL MODEL AND IMPEDANCE CALCULATION

The impedance of a multi-layered (sandwich) radome can be calculated using a stepped transmission line analogy. The impedance of the region on the exterior of the

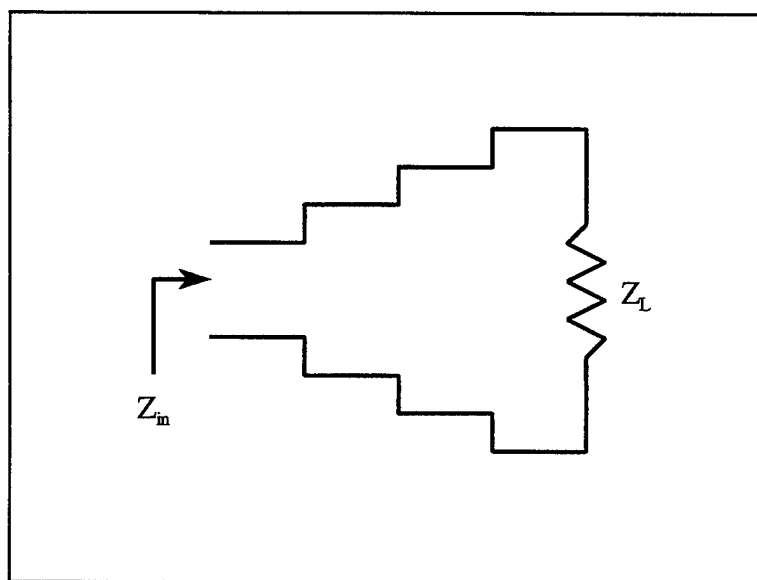


**Figure 2.2** Stepped impedance transformer

radome,  $Z_L$ , is transformed through each layer until the region on the interior side is reached. This transformed impedance,  $Z_{in}$ , is the impedance that is presented to a plane wave incident on the radome. The schematic representation of a sandwich radome is shown in Figure 2.2. To apply the transmission line model to the radome, we first define the quantities shown in Figure 2.3. Each layer  $n$  has a thickness,  $t_n$ , and a relative dielectric constant,  $\epsilon_n$ . The exterior region has the highest index and the interior region the lowest. The exterior is region

number  $N$ , so there are  $N-2$  layers of radome material. Let  $\eta_n$  be the intrinsic impedance of the layer  $n$  and  $Z_n$  be the wave impedance looking into the layer  $n$  at an incidence angle  $\theta_n$ .

For perpendicular polarization

$$Z_n = \frac{\eta_n}{\cos \theta_n} \quad (2.7)$$

and for parallel polarization

$$Z_n = \eta_n \cos \theta_n. \quad (2.8)$$

$\hat{Z}_n$  is the transformed impedance that is seen looking through a sandwich of layers as shown in Figure 2.3. The transformed impedance is

$$\hat{Z}_n = \eta_n \left[ \frac{\hat{Z}_{n+1} + Z_n \tanh(\gamma_n t_n)}{Z_n + \hat{Z}_{n+1} \tanh(\gamma_n t_n)} \right] \quad 1 \leq n \leq (N-1) \quad (2.9)$$

where as in [Ref. 5]

$$\eta_n = \sqrt{\frac{\mu_o}{\epsilon_{r_n} \epsilon_o}} \quad (2.10)$$

$$\gamma_n = \alpha + j\beta = j\omega \sqrt{\mu_o \epsilon'} \left( 1 - j \frac{\epsilon''}{\epsilon'} \right)^{\frac{1}{2}} \quad (2.11)$$

$$\epsilon = \epsilon' - j\epsilon'' \quad \epsilon' = \epsilon_0 \epsilon_r. \quad (2.12)$$

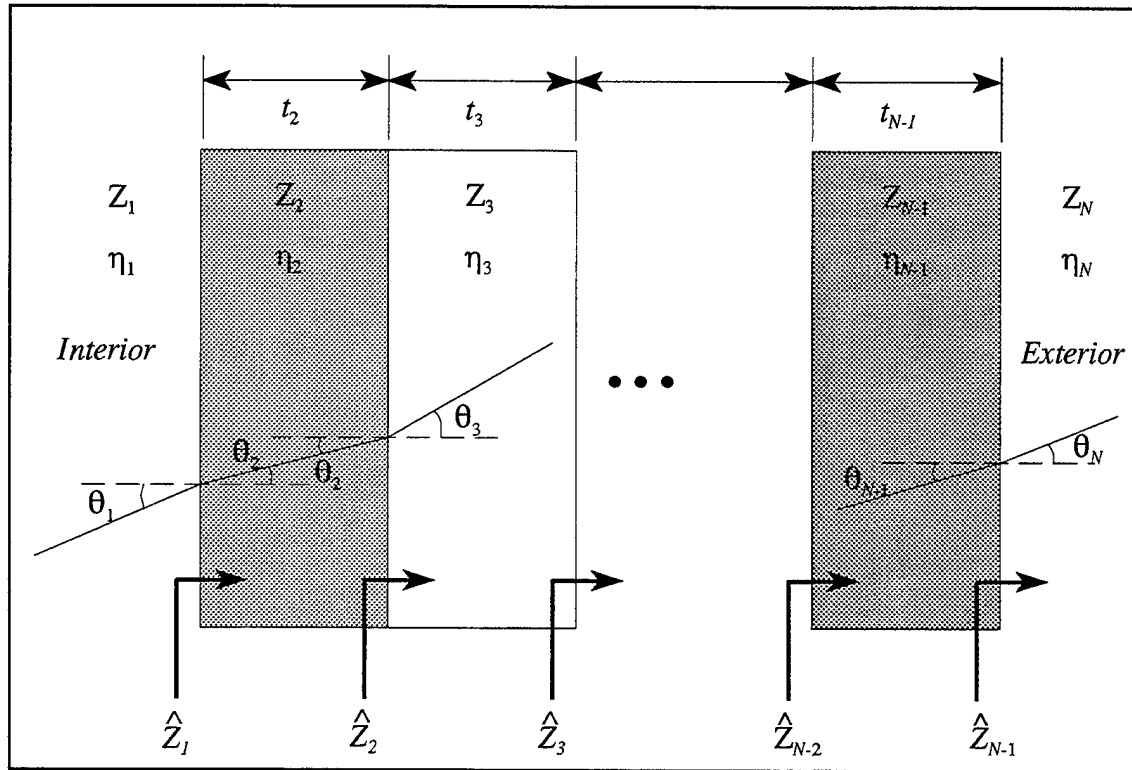


**Figure 2.3** Multi-layered radome wall geometry

The input impedance is computed by transforming the free space load of the exterior back to the interior surface. An input impedance is computed at each interface and then used as a load to be transformed back to the previous interface [Ref. 6]. This is repeated until  $\hat{Z}_n$  is computed for the final layer.

The change in incidence angle at the interface between materials with different dielectric constants (refraction) can be determined by using a form of Snell's Law. This is expressed as

$$\sin \theta_{n+1} = \sqrt{\frac{\epsilon_{r_n}}{\epsilon_{r_{n+1}}}} \sin \theta_n \quad \text{or} \quad \sin \theta_{n+1} = \frac{\eta_n}{\eta_{n+1}} \sin \theta_n . \quad (2.13)$$

If necessary, an equivalent single layer radome (denoted by the subscript  $e$ ) can be derived from a multiple layer radome by using the equation

$$Z_{in} = Z_e \left[ \frac{Z_o + Z_e \tanh(\gamma_e t_e)}{Z_e + Z_o \tanh(\gamma_e t_e)} \right] . \quad (2.14)$$

Since  $Z_{in}$  is complex,  $Z_e$  and the product  $\gamma_e t_e$  can be determined.

Once known, the impedance  $Z_{in}$  can be used to solve for the reflection coefficient seen by an incident wave

$$\rho = \frac{Z_{in} - Z_o}{Z_{in} + Z_o} . \quad (2.15)$$

When  $Z_{in}$  and  $Z_o$  are equal,  $\rho = 0$ , and all energy is transmitted. When there is a large difference between  $Z_{in}$  and  $Z_o$ ,  $|\rho| \rightarrow 1$ , and a large reflection results. Hence, the best radomes have impedances that are close to the intrinsic impedance of free space, approximately 377 ohms.

The PATCH and RADOME programs require radome impedance as an input parameter. For a sandwich wall, the value can be calculated from Equation 2.9. The impedance is allowed to change as a function of position on the radome, but it is assumed constant with angle. Using a computer program (see Appendix C) to calculate  $Z_{in}$  for a range of incidence angles, an estimate of the radome impedance was obtained that was relatively constant over a broad range of incidence angles. An average value of impedance was chosen for each of the radomes measured and used in the computer simulations.

Two particular radomes were used for testing and analysis in this thesis: (1) an AGM-88 HARM, and (2) an AIM-9C. The cross sectional geometry for the walls are shown in Figures 2.4 and 2.5, respectively. The computer generated impedances for the HARM radome are shown in Figure 2.6. The impedance is relatively constant over the range  $0^\circ \leq \theta \leq 50^\circ$ . From the geometry of the HARM radome and the antenna, it was determined

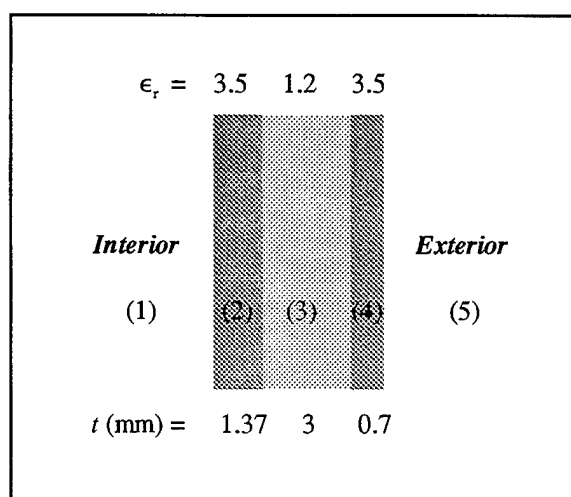


**Figure 2.4** HARM radome wall

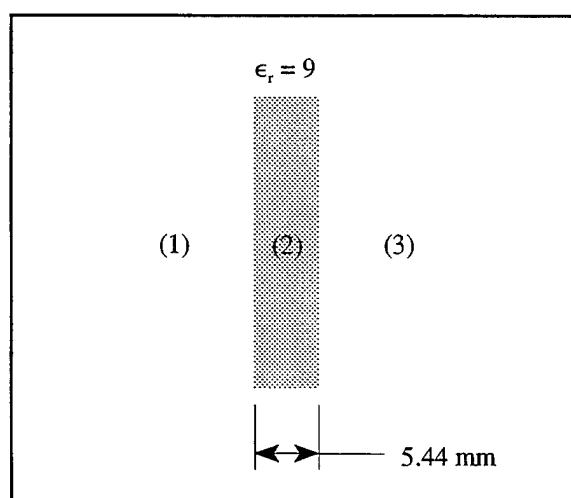


**Figure 2.5** AIM-9C radome wall



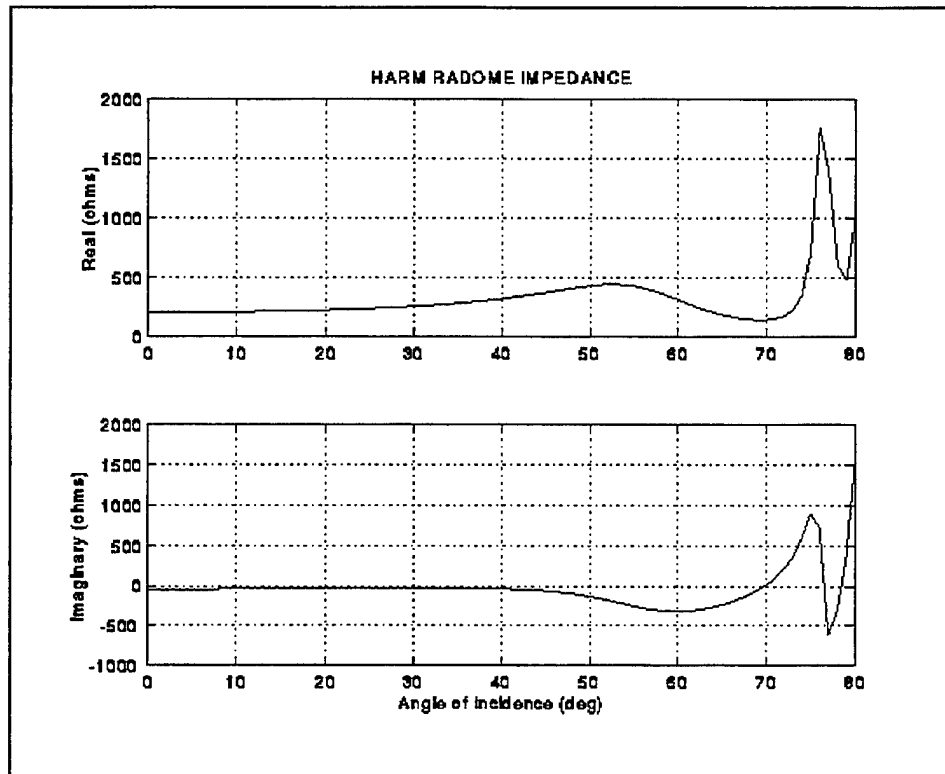


**Figure 2.6** HARM radome impedance as a function of incidence angle

that the average incidence angle along the surface of the radome was approximately 35°. Thus, an impedance of  $278 - j31$  ohms was used in the computer simulations. For the AIM-9C radome, the impedance calculation was simplified due to the presence of just one layer and nearly normal incidence around the hemispherical surface. Using Equation 2.9, the AIM-9C impedance was  $234 - j166$  ohms. The impedance values for both radomes are listed in Table 2.1.

**Table 2.1** Radome Impedance Used in the Computer Calculations

Radome	Material	Complex Impedance
HARM	Fiberglass composite	$278 - j31$ ohms
AIM-9C	Alumina	$234 - j166$ ohms

### C. PATCH AND RELATED PROGRAMS

The program PATCH was produced by Sandia National Laboratories in 1988 [Ref. 4]. It is a FORTRAN program that uses the method of moments to calculate electromagnetic fields from scattering and radiating bodies. PATCH performs the electromagnetic calculations, while a collection of pre- and post-processing programs are available for generating, formatting, converting, and error checking the input and output of the PATCH program. A brief description of each program is given in Table 2.2. The programs and their relationships are shown in Figure 2.7. Most of the programs<sup>1</sup> were generated at the Naval Postgraduate School to allow automatic meshing of bodies built in AutoCAD and to translate the meshed surfaces to PATCH input format.

During execution, PATCH reads an input file with geometry and calculation parameters. Either of two commercial computer aided drawing (CAD) programs, AutoCAD or ACAD, can be used to specify a shape. These programs are extremely versatile, and are unlimited in the scope of geometries that can be generated. Files can be transferred between the two using the IGES format. Whether the shape is generated in AutoCAD or ACAD, the later program is used to construct a shell mesh, which is written in ACAD's "facet" format. Meshing results in a discretized body composed of triangular facets. For example, a simple rectangular plate is shown in Figure 2.8. The degree of fineness (or coarseness) of the mesh is determined by specifying the number of facets, or edges, along the horizontal and vertical

---

<sup>1</sup>Commercially available program names are in ALL CAPITALS, locally generated programs are in **boldface**, and input/output files are in *italics*. Locally generated programs have various authors, and have been modified to suit individual users.

**Table 2.2** Summary of PATCH and related processing programs

Name	Brief Description	Source
AutoCAD	CAD drawing program	Autodesk
ACAD	CAD program capable of auto meshing surfaces	Lockheed-Martin (Ft. Worth, TX)
<b>pta.x</b>	PATCH-to-ACAD data translator	NPS
<b>atp.x</b>	ACAD-to-PATCH data translator	NPS
<b>knit.x</b>	Checks PATCH data files for duplicate edges and nodes	NPS
<b>bldmat.x</b>	Generates MATLAB “.m” files for plotting geometry using PATCH data files	NPS
<b>pltpatch.m</b>	A MATLAB program that plots the geometry files generated by <b>bldmat.x</b>	NPS
<b>combine.m</b>	A MATLAB program that combines separate geometry files into one object for use in PATCH	S.M. Herzog
BUILDN5.X	PATCH preprocessor to generate input geometry files and specify calculation parameters	Sandia National Laboratories
PATCH ( <b>patch2v.x</b> )	Numerical electromagnetics code that computes scattered and radiated fields using the method of moments.	Sandia National Laboratories

sides. As a rule of thumb, the lengths of the individual edges should be approximately one tenth of a wavelength ( $0.1\lambda$ ). For larger bodies, this means a large number of elements, and a correspondingly larger facet file.

The facet file generated by ACAD must then be converted to PATCH text format. This is accomplished by the program **atp.x** (ACAD to PATCH). The program **pta.x** performs the reverse data translation. The PATCH version of a facet file defines the

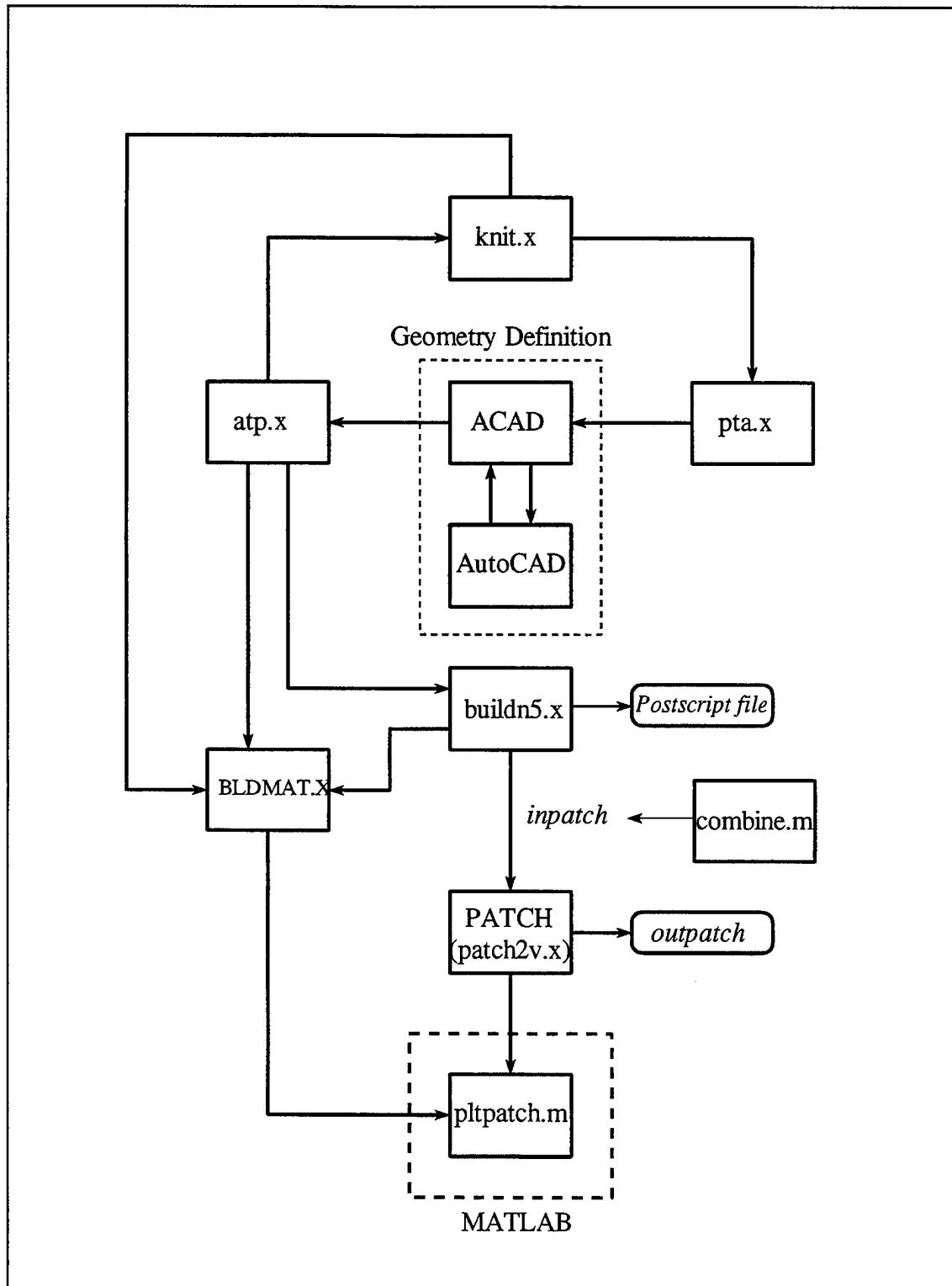


**Figure 2.7** Relationships between PATCH and its pre- and post-processing programs

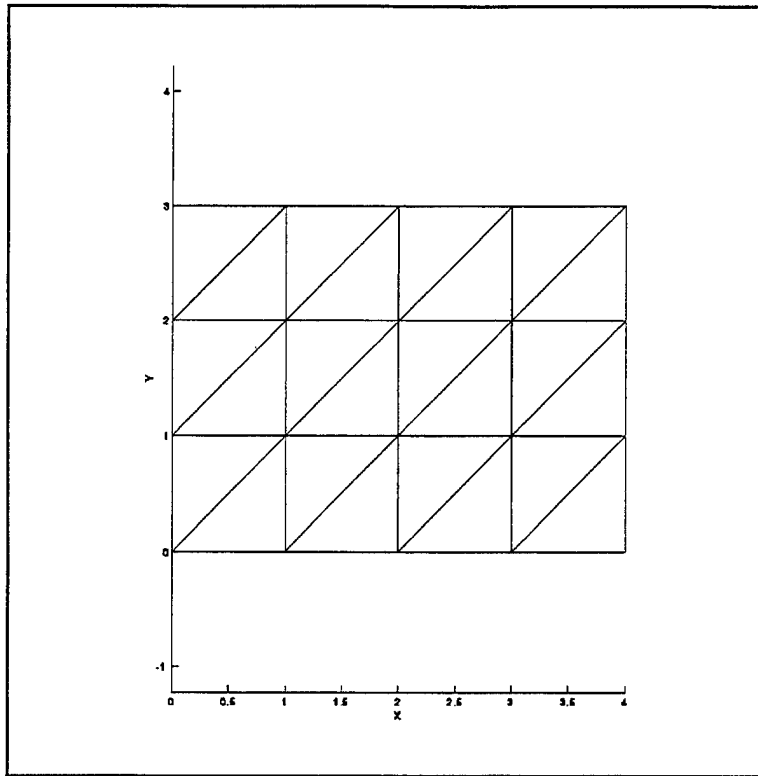


**Figure 2.8** Plate composed of triangular facets

geometry in terms of nodes and edges. Nodes are listed with their respective Cartesian coordinates, and edge segments are listed with their two defining nodes. An example of this will be presented later. The output of **atp.x** is used in the program **BUILDN5.X**, which constructs the final ASCII input file that **PATCH** will read. When **BUILDN5.X** is executed, it prompts the user to specify the input geometry file, which is the converted facet file from **atp.x**. If no input file is available, simple geometries such as quadrilaterals, disks, or spheres can be generated by **BUILDN5.X**. The program then asks for a set of simulation parameters that define the particular calculations to be performed. At this point the excitation voltages and currents, surface impedances, frequencies, and observation points are entered. The program **BUILDN5.X** compiles all of this information and constructs an ASCII file properly

formatted for use in PATCH. This file must be renamed *inpatch* before PATCH is executed. A sample *inpatch* file for the mesh in Figure 2.8 is listed in Appendix A. The program BUILDN5.X is also capable of displaying the geometry on the screen or writing a postscript file. However, geometry display requires the DISSPLA graphics software package.

When PATCH is executed, a number of output files are generated. *Outpatch* is a data summary that includes a listing of all the input parameters, geometry (nodes and edges), and the computed fields and currents. Three additional files, *ampp.m*, *ampt.m*, and *ang.m* are saved with *.m* extensions for use in MATLAB. These files contain the calculated radiation pattern data, as noted in Table 2.3. MATLAB is the primary means by which the calculated pattern data is displayed. The *.m* files are simply loaded into a plotting routine to view the data points.

Other PATCH related programs include **bldmat.x**, **knit.x**, and **combine.m**. The program **bldmat.x** enables a display of the mesh model in MATLAB. The program converts the ASCII facet file (from **atp.x** or BUILDN5.X) to *.m* files. The MATLAB routine **pltpatch.m** is then used to display the geometry. **Combine.m** appends one geometry file to another so that successive nodes and edges are numbered in sequence.

There are occasions when the facet files generated by ACAD/AutoCAD contain redundant points or edges. The program **knit.x** is an error checking routine that removes duplicate edges and checks for other file errors. This program provides a means to remove bad data and generate a new error-free data file.

#### D. RADOME PROGRAM

The FORTRAN program RADOME is used to compute the pattern of an antenna radiating in the presence of an axially symmetric radome. This code also uses the method of moments, and was originally developed by Francis [Ref. 2] and later improved by Klopp [Ref. 3]. See also [Ref. 7]. The code is essentially self contained and does not require the geometry preprocessing that PATCH does. RADOME is restricted to axially symmetric bodies of revolution (BOR) such as cones, disks, spheres, hemispheres, paraboloids, cylinders, and ogives. These basic shapes can be generated internally by RADOME. Other generating curves can be specified in the file *radinp*, which is simply a two-column table of surface coordinates  $\rho$  and  $z$ . RADOME produces three output files that are saved with a *.m* file extension for plotting in MATLAB (see Table 2.3). For bookkeeping purposes, the underscore character in the filenames is occupied by a letter character that identifies the run. Just as in the case of PATCH, each observation angle in *ang\_.m* has a corresponding pattern value in *eppol\_.m* and *etpol\_.m*.

**Table 2.3** Output files for PATCH and RADOME

PATCH output files	RADOME output files	Description
<i>ang.m</i>	<i>ang_.m</i>	Azimuth observation angles ( $\theta$ points)
<i>ampp.m</i>	<i>eppol_.m</i>	$E_\phi$ ( $\phi$ -polarized E-field component, in dB)
<i>ampt.m</i>	<i>etpol_.m</i>	$E_\theta$ ( $\theta$ -polarized E-field component, in dB)

### III. COMPUTER CODE VALIDATION

#### A. APERTURE MODEL

In order to validate the results of the PATCH and RADOME programs, we need to accurately model the antenna used in the anechoic chamber measurements. Details of the chamber facility are discussed in Chapter IV. For all of the experimental data that was gathered, a Microline 56X1 Standard Gain Horn was used as a receive antenna. This horn has an exponential taper in both the E- and H-planes as depicted in Figure 3.1. Typically, this type of horn is used in the detection and measurement of microwave power. Additional specifications for the horn are given in Table 3.1. The low voltage standing wave ratio (VSWR) is crucial to laboratory measurements since it prevents undesirable reflection at the

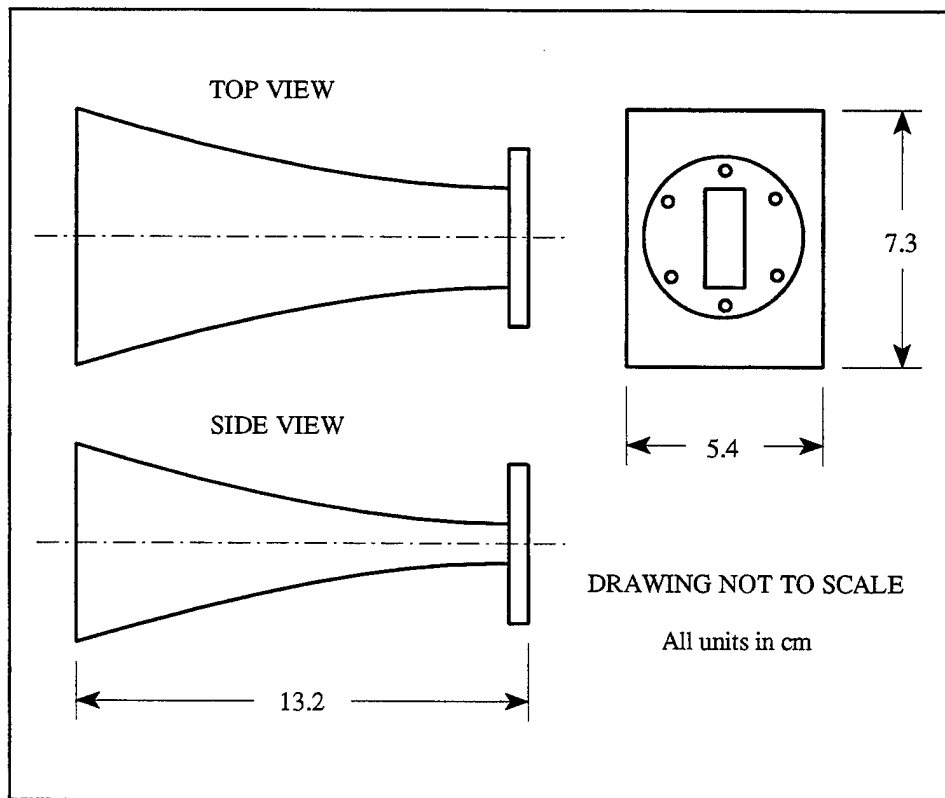


Figure 3.1 Microline 56X1 standard gain horn



antenna input which could possibly add constructively or destructively with radome reflections, thereby producing misleading data.

**Table 3.1** Microline 56X1 Specifications

Frequency Range	Nominal Gain	Frequency at Nominal Gain	Gain Variation over Frequency Band	Accuracy	Maximum VSWR
8.2 - 12.4 GHz	17 dB	11.0 GHz	+/- 1.5 dB	+/- 0.3 dB	1.15

### 1. Patch Code Antenna Model

In order to simulate the 56X1 horn in PATCH, a model of the antenna aperture was developed based on slots in a conducting sheet. The excitation amplitude of the slots is obtained by sampling the  $TE_{10}$  mode distribution which is approximately the distribution in the horn aperture. A rectangle approximating the size of the actual horn aperture ( $5.4 \times 7.3$  cm) was subdivided into a  $12 \times 13$  grid of smaller squares, which in turn were divided into two faces by the addition of a diagonal. At 10 GHz, which is the test frequency for all measurements, the smaller squares are  $0.2\lambda$  (0.6 cm) in dimension. This allows the individual element to be electrically small while keeping the grid from becoming too dense. The aperture grid is shown in Figure 3.2.

The next step is to determine the voltage excitation at each slot. If a voltage is applied across a small horizontal slit in a conductive material, the resulting far field pattern will have

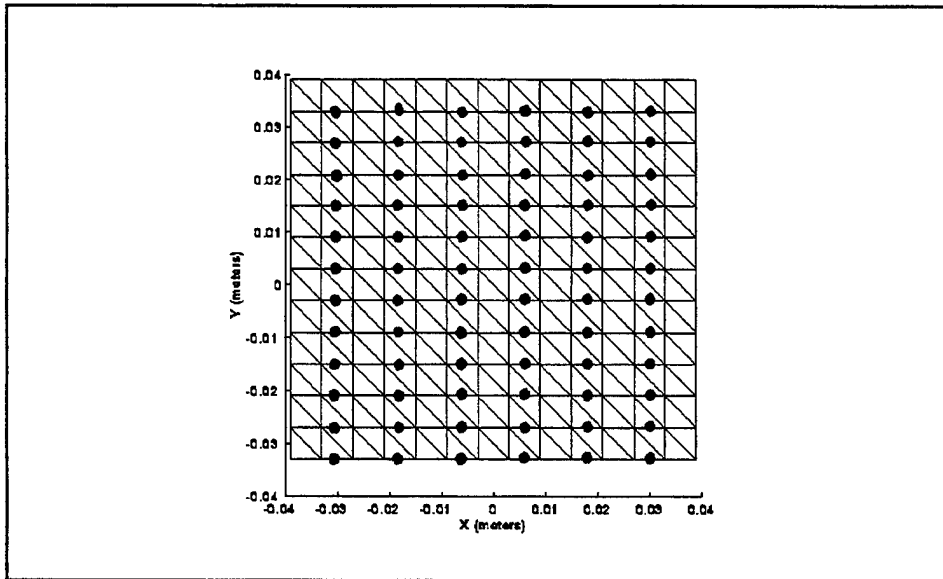


**Figure 3.2** Aperture model for Microline 56X1 antenna

a vertical E-plane ( $y$ ) and a horizontal H-plane ( $x$ ). An array of slits with varying voltage amplitude and phase excitations can be used to control the array far field pattern characteristics. The larger the array becomes in the horizontal direction, the narrower the H-plane beamwidth. And conversely, the larger the array in the vertical direction; the narrower the E-plane beamwidth. For the Microline antenna model, a total of 72 horizontal edges were chosen as slits. These are denoted by small dots in Figure 3.2. The extra row of squares at the top is required to specify the polarization of the slits just below. The size of the aperture and the pattern of slits were adjusted until the computed pattern agreed with the measured 56X1 pattern in gain and beamwidth.

Because of  $TE_{10}$  waveguide excitation imperfections and the horn flare, the aperture plane of the 56X1 does not have uniform illumination with constant phase. The actual illumination can be modeled by a cosine on a pedestal function as shown in Figure 3.3. The pedestal value, or illumination present at the edge, is  $A$ , and the width of the aperture is  $a$ .

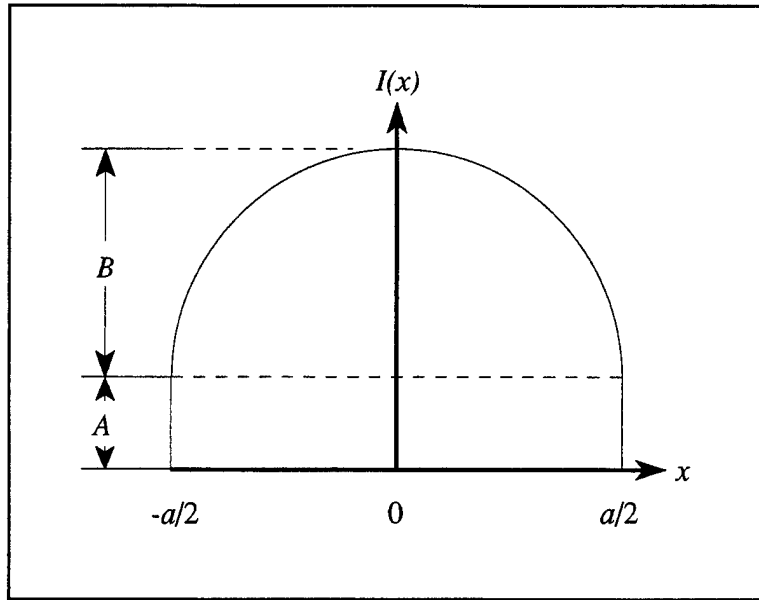


**Figure 3.3** Cosine on a pedestal

Mathematically, the curve is expressed by

$$I(x) = A + B \cos\left(\frac{\pi x}{a}\right) \quad (3.1)$$

with  $A + B = 1$ . The illumination tapering in the 56X1 is a result of the horn's curved shape.

This is done primarily to keep the input VSWR low [Ref. 8].

An aperture phase error occurs also as a result of the flare geometry. The wave fronts that originate at the waveguide entrance are spherical in shape. When these wave fronts cross the flat exit plane of the large end of the horn, the center of the wave is ahead of the outer edges. Across the exit plane, the phase varies as

$$e^{j\left(\frac{2x}{a}\right)^2 \psi_x} \quad (3.2)$$

where  $\psi_x$  is the maximum *quadratic phase error* at the edge of the aperture, in radians.

Together, the cosine taper and phase error produce an illumination in the horizontal direction which is expressed as

$$I(x) = \left[ A + B \cos\left(\frac{\pi x}{a}\right) \right] e^{j\left(\frac{2x}{a}\right)^2 \psi_x} . \quad (3.3)$$

Tapering in the vertical direction is expressed by substituting  $y$  for  $x$  and  $b$  for  $a$  in Equations 3.1 through 3.3. Since the taper and phase error in the vertical direction is not necessarily the same as the horizontal direction, the constants  $A$  and  $B$  will not be the same, and  $\psi_x$  will be replaced by  $\psi_y$ .

Applying the illumination function to the aperture model, Equation 3.3 is sampled at the slit locations to obtain the array excitation. Different values for the pedestal and phase error were investigated until there was satisfactory agreement with the measured 56X1 antenna pattern. A program for defining a two-dimensional tapered array of voltages is listed in Appendix B. The effect of increasing the taper ( $B > A$ ) is to reduce the side lobe level and increase the beamwidth. The effect of increasing the phase error is to fill the pattern nulls between the main beam and side lobes. Beamwidth is not significantly affected for small values of  $\psi_x$ . The pattern effects are illustrated in Figures 3.4 and 3.5.

After numerous iterations, the best agreement with measured data from the 56X1 horn occurred with E-plane taper values of  $A = 0.6$ ,  $B = 0.4$ , and  $\psi_x = 35^\circ$  (denoted by 0.6/0.4/35°). The corresponding best H-plane parameters were chosen as 0.1/0.9/70°. The patterns for both planes are shown in Figures 3.6 and 3.7. The agreement is good in the main beam, with

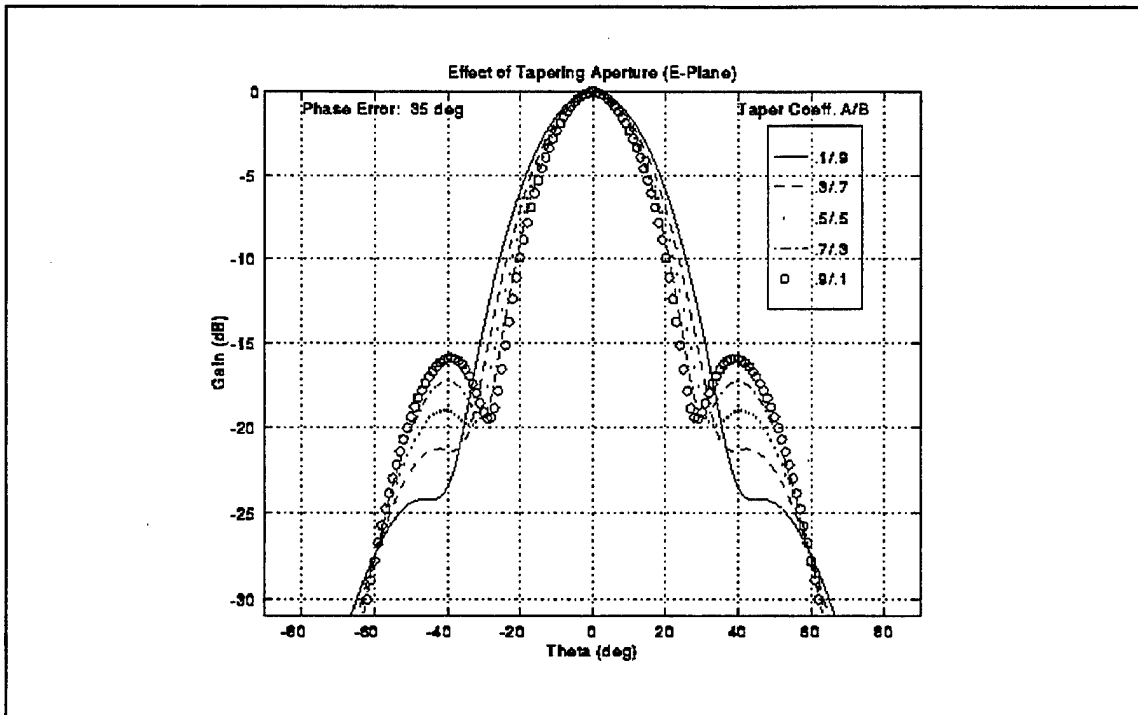


Figure 3.4 Effect of tapering

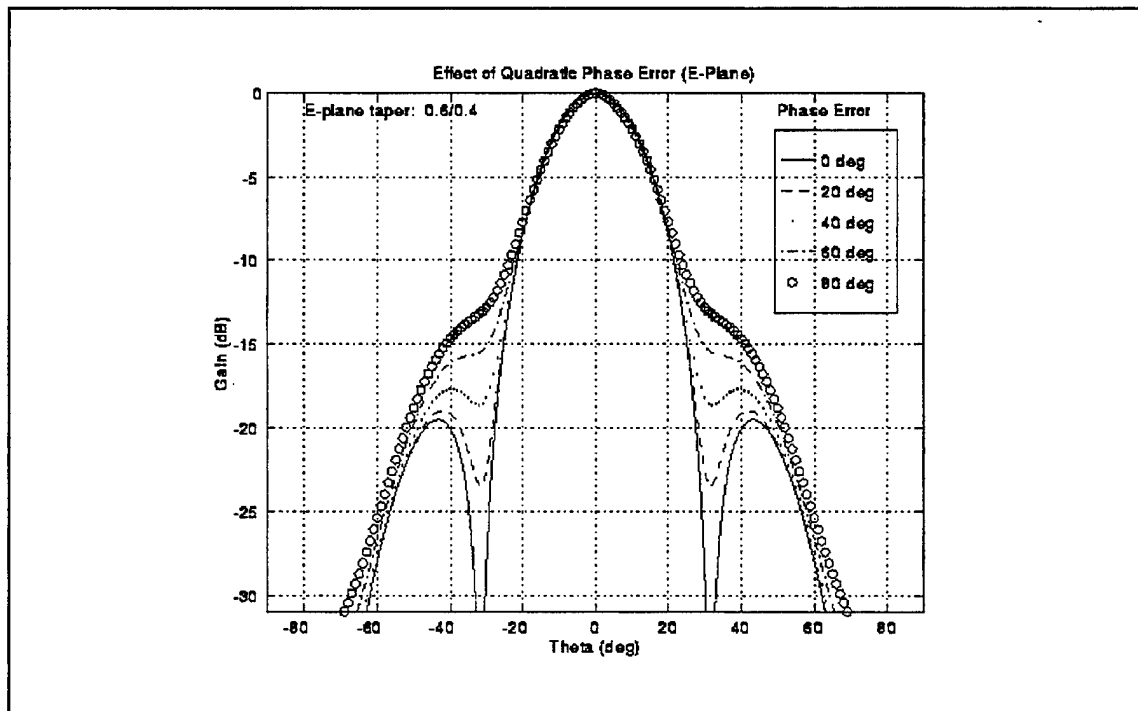
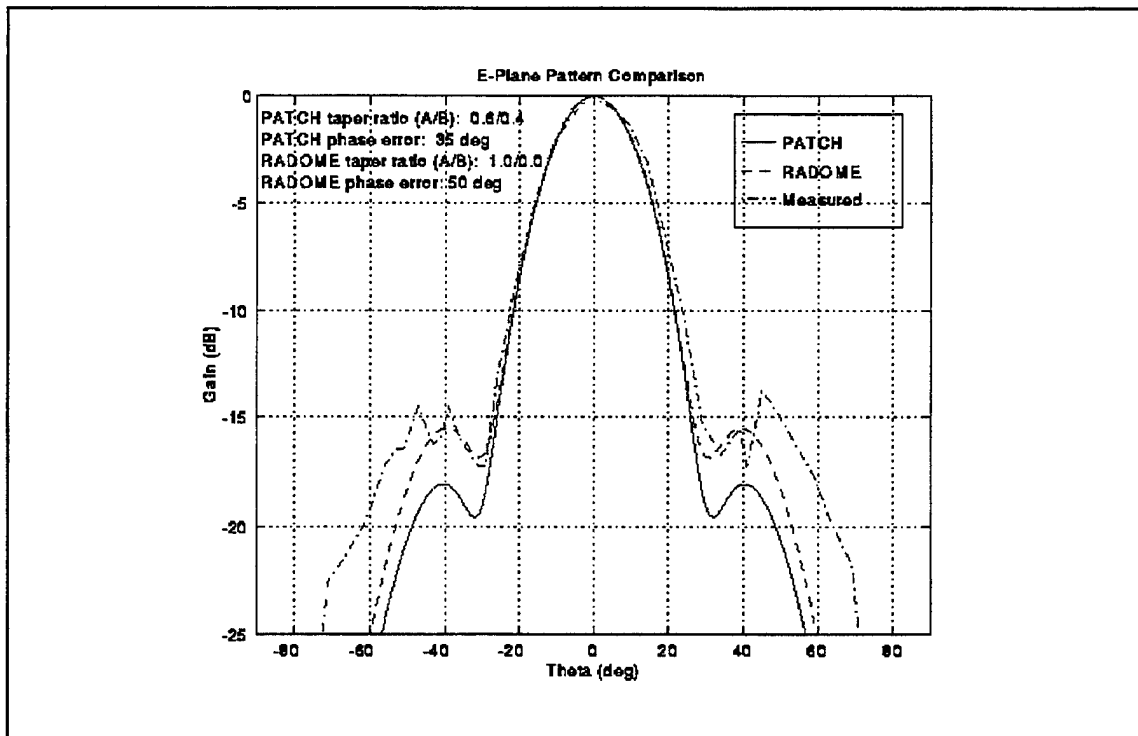
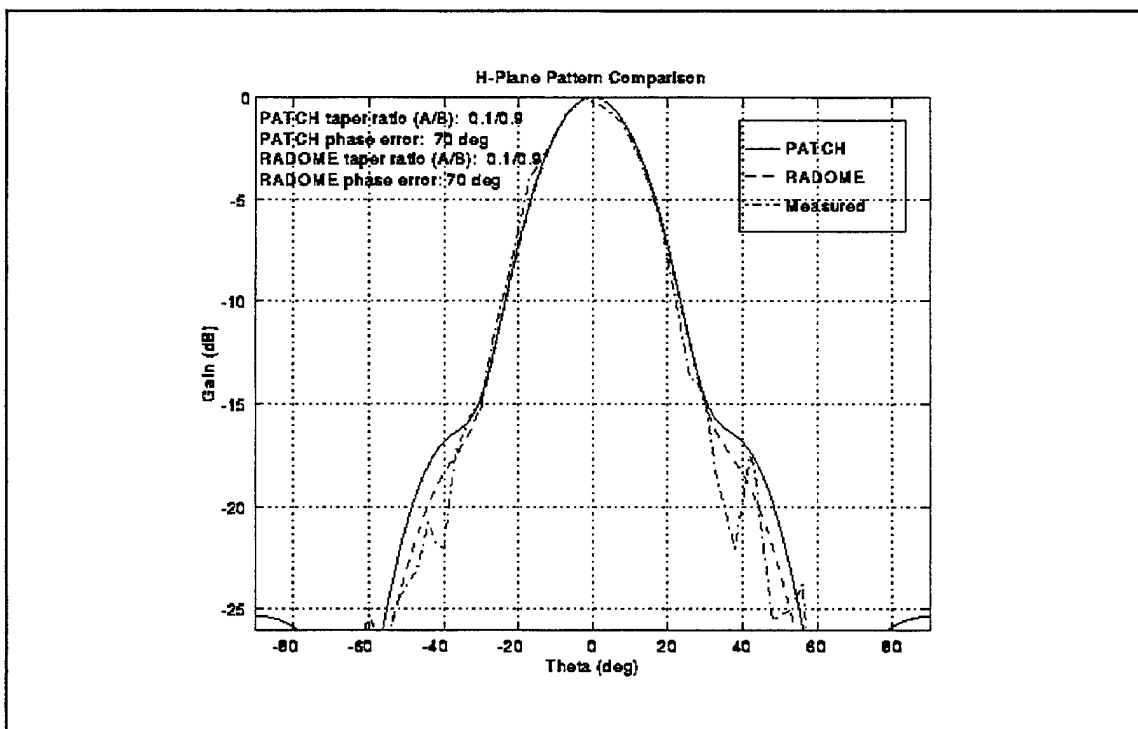


Figure 3.5 Effect of quadratic phase error

about 2 dB difference in the side lobe level for PATCH. This is to be expected due to the sampling nature of the model itself. For the simulations using radomes, the aperture model described above is used as a reference. By comparing these patterns with those obtained with the radome present, the effect of the radome can be deduced.



**Figure 3.6** Comparison of main beam E-plane patterns



**Figure 3.7** Comparison of main beam H-plane patterns

## **2. Radome Code Antenna Model**

The code RADOME can handle circular or rectangular antenna apertures of arbitrary illumination. The antenna pattern is computed by integrating the specified distribution at a given spherical coordinate location ( $R, \theta, \phi$ ). No approximations are made in the calculation other than numerically evaluating the integrals.

When using a rectangular aperture, the RADOME program asks for the antenna dimensions in wavelengths. At 10 GHz, the 56X1 horn is  $1.8 \times 2.4$  wavelengths. In order to match the output with the measured data, the dimensions and distribution were adjusted. As in the PATCH model, the program was modified to accommodate tapering and quadratic phase error. The beamwidths were matched in RADOME using an aperture of  $2.0 \times 2.6$  wavelengths. The values used for  $A, B$ , and  $\psi_x$ , respectively, are  $1/0/50^\circ$  for the E-plane and  $0.1/0.9/70^\circ$  for the H-plane. The resulting patterns are shown in Figures 3.6 and 3.7. There is good agreement with the 56X1 measured data. Furthermore, for the purpose of radome evaluations, there is satisfactory agreement between the patterns produced by RADOME and PATCH. This demonstrates that when modeling the same antenna with both programs, there is some correlation in the required tapers and phase errors and similar results are achieved.

### **B. SCATTERING DISK TEST CASE**

The data in Figures 3.6 and 3.7 show that both the RADOME and PATCH antenna models agree with measured data when radiating in free space. When a radome is present, some waves scattered by the radome can return to the antenna and be either received or



rescattered. This interaction between the antenna and radome can affect the side lobe level of the transmitted field, especially at wide angles. The RADOME code does not include these multiple reflections between the antenna and radome, but PATCH does. The strength of the antenna reflection in PATCH can be controlled somewhat by varying the surface impedance on the aperture array plate.

A good test case for evaluating the effects of multiple reflections is to place a perfectly conducting (PEC) disk in front of the aperture and compare the results for both codes. The geometry is shown in Figure 3.8. The diameter of the disk is  $2\lambda$ , and it is positioned  $5\lambda$  in front of the aperture.

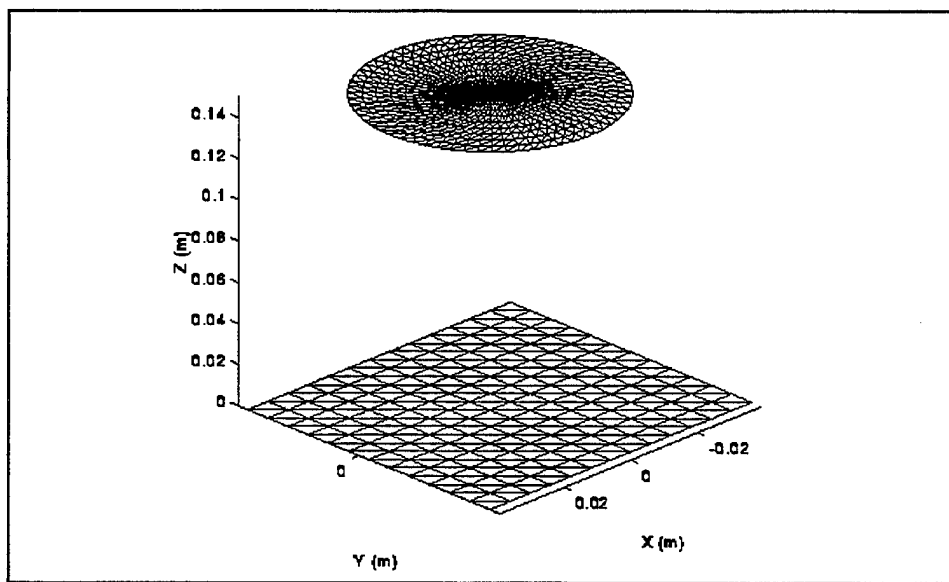


**Figure 3.8** PEC disk in front of aperture

The resulting patterns are shown in Figure 3.9. The patterns from the main beam up to the fourth side lobe agree very well ( $0 < \theta < 80^\circ$ ). The PATCH array plate impedance is 10,000 ohms, which makes it essentially invisible to fields scattered from the disk. Beyond

$\theta = 90^\circ$ , PATCH gives a number of additional lobes due to the disk scattered field adding and canceling with the array field. RADOME has no antenna field in the rear hemisphere, and thus the pattern in this region is determined solely by the disk scattered field. Figure 3.9 indicates that interactions between the antenna and disk are not significant in the range  $0^\circ < \theta < 90^\circ$ , which is expected because the antenna models are transparent to waves scattered from the disk.

In order to test the multiple reflection effects, PATCH was run with different impedance conditions on the aperture plate. The surface impedance of the aperture was varied from 1,000 to 20,000 ohms, with and without the disk present. For the first case (aperture alone), the results are shown in Figure 3.10. There is virtually no change in the H-plane pattern, and only a small change in the E-plane pattern when the aperture surface impedance is varied.

The second case has the aperture with the PEC disk. Again the surface impedance of the aperture plate was varied, and the resulting patterns are shown in Figure 3.11. This case is more interesting in that the surface impedance of the aperture is important with regard to multiple reflections between the two structures. The patterns show that the aperture is relatively transparent for impedances of 1,000 to 20,000 ohms, demonstrated by the fact that these curves are grouped together. When the aperture is a PEC, we see the pattern diverges from the others as a consequence of waves being reflected back and forth between the aperture and disk.

In summary, the PATCH code allows a wide range of antenna surface impedances which directly affect the strength of the interaction between the antenna and scattering body.

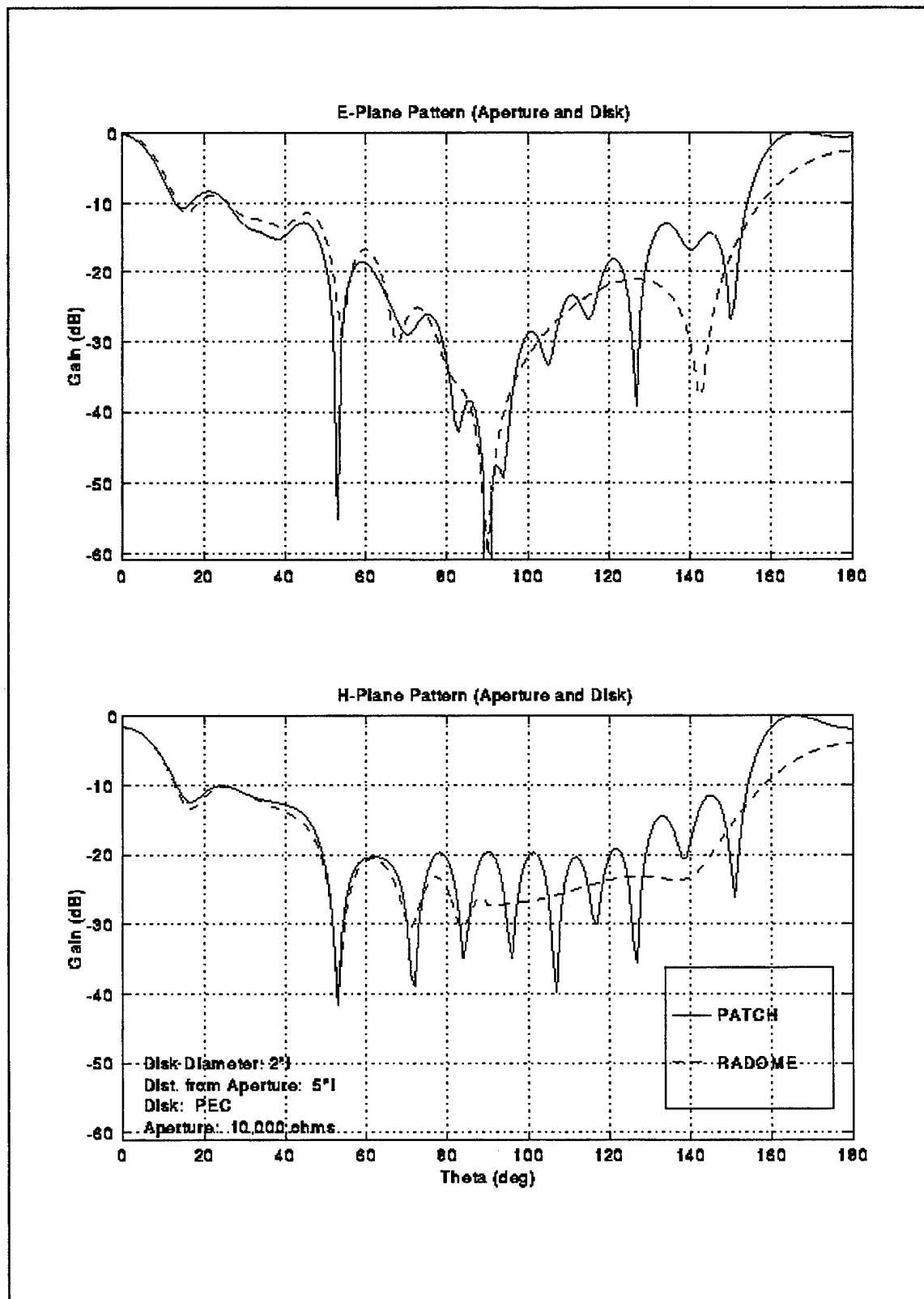


Figure 3.9 Patterns with aperture and disk

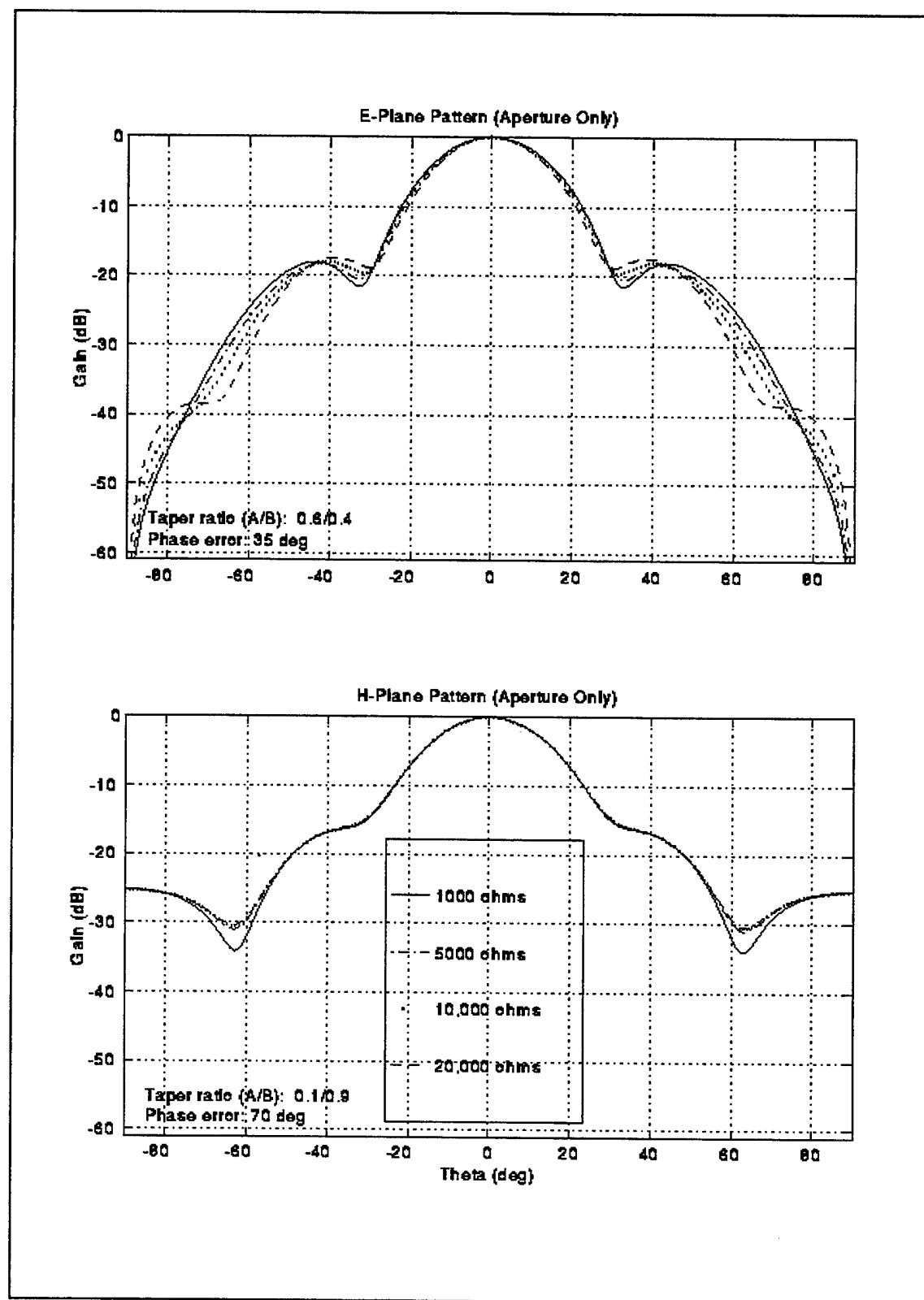


Figure 3.10 Effect of antenna surface impedance on the aperture pattern

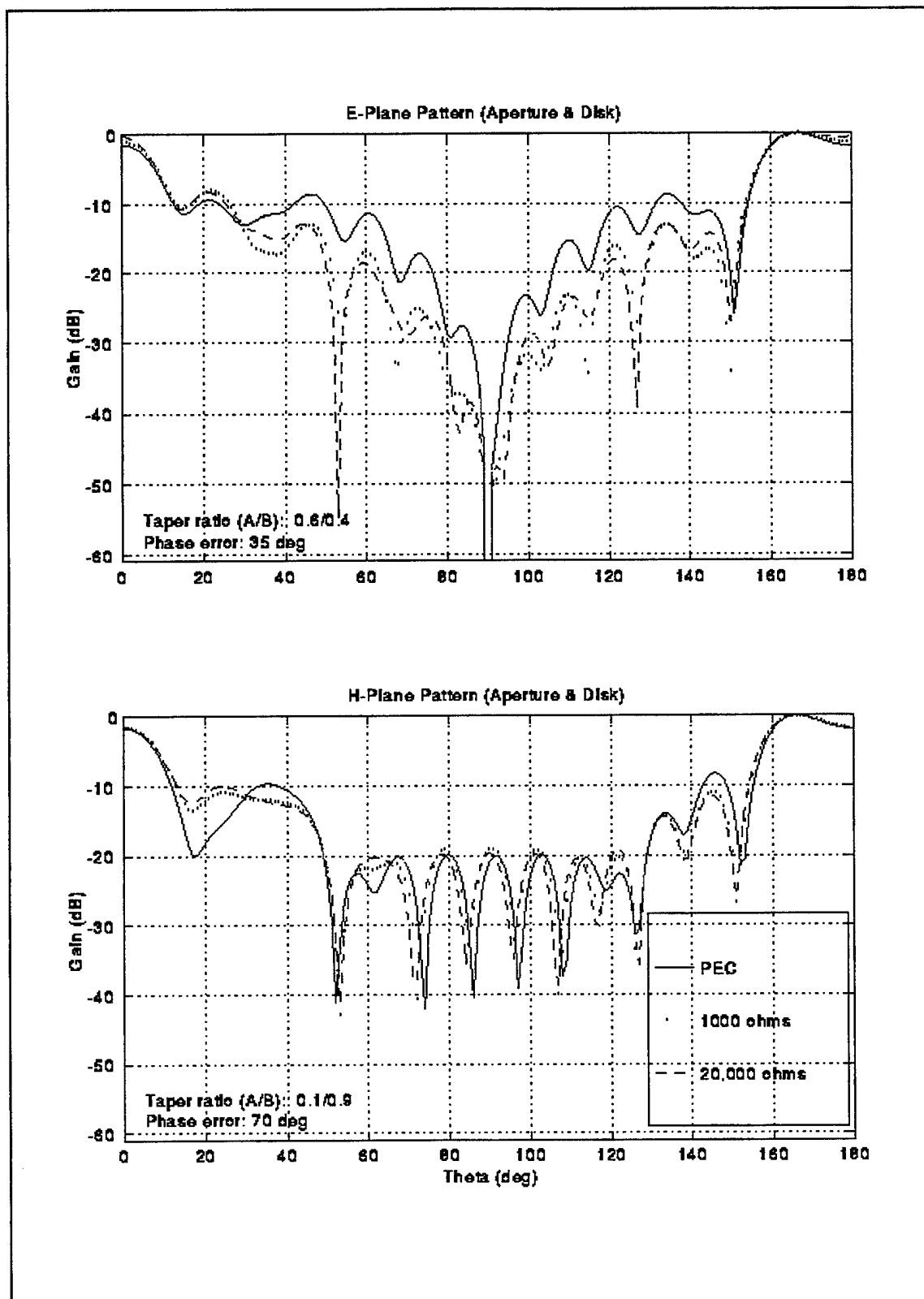


Figure 3.11 Effect of antenna surface impedance on the aperture and disk pattern





## IV. DATA ANALYSIS

### A. ANECHOIC CHAMBER FACILITY

The Naval Postgraduate School's anechoic chamber was used for all measurements presented in this thesis. The chamber is approximately 25 feet long, 12 feet wide, and 10 feet high. A Hewlett-Packard X890A microwave horn serves as the transmit antenna at one end of the chamber. The geometry of this E-plane sectoral horn is shown in Figure 4.1. A rotating pedestal is located approximately 19 feet from the transmit antenna. The pedestal holds the receive antenna (Microline 56X1) and test radome, and is capable of rotating

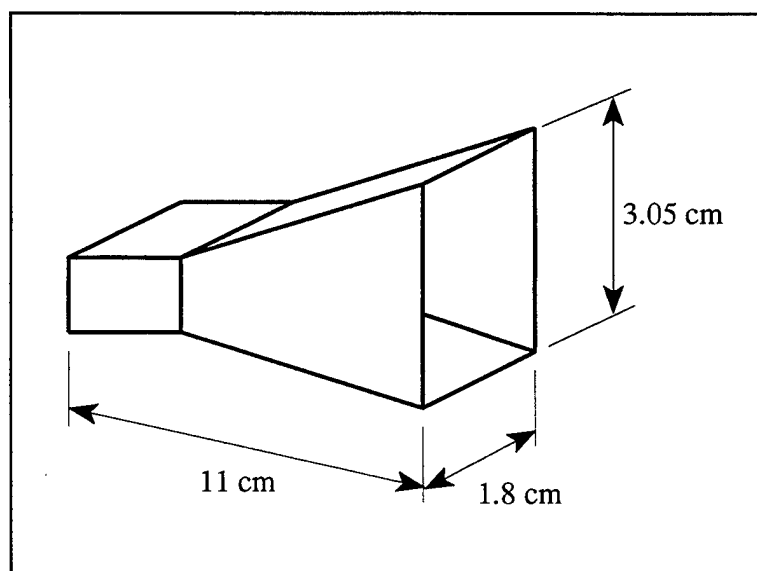


**Figure 4.1** HP X890A microwave horn

through 360° in azimuth. Both of the antennas are fed by coaxial cable via WR-90 waveguide adaptors. The chamber walls, floor, ceiling, and pedestal are covered with carbon-based radar absorbent material.



The measurement system uses a microwave amplifier, synthesized sweeper, frequency converter, and network analyzer to generate, detect, and process microwave signals. The pedestal servo motor and network analyzer are connected to a personal computer that serves as the main controller/interface for the chamber. A schematic of the chamber equipment is shown in Figure 4.2.

Measurements were taken for  $-90^\circ \leq \theta \leq 90^\circ$ , with  $\theta = 0^\circ$  pointing directly at the transmit antenna. Data was not recorded for angles beyond  $\theta = \pm 90^\circ$ , since the receive antenna faces the rear of the chamber in this sector. In practice, the radiation pattern will be close to zero because of the missile body. Using Labview 3.0 software to control the instrumentation, data was recorded for a transmit frequency of 10 GHz at  $1^\circ$  increments. The recorded signal is an average of 32 samples taken at each azimuth angle. Sampling reduces the effect of noise and provides more repeatable data.

## **B. PHASE CENTER FOR MICROLINE 56X1 HORN**

In the far field of a microwave horn antenna, it is desirable to assign a reference point for a given frequency such that the phase of the radiated wave is independent of  $\theta$  and  $\phi$ . This point is called the *phase center* of the antenna. When viewed from a far field observation point, the wave fronts radiated by the antenna are spherical waves that appear to originate from the location of the phase center [Ref. 9].

A graphical method of obtaining the phase centers for E- and H-plane sectoral horns is given in [Ref. 9]. For a given frequency and flare angle, the phase center distance is obtained from a graph. An average flare angle was determined for the E- and

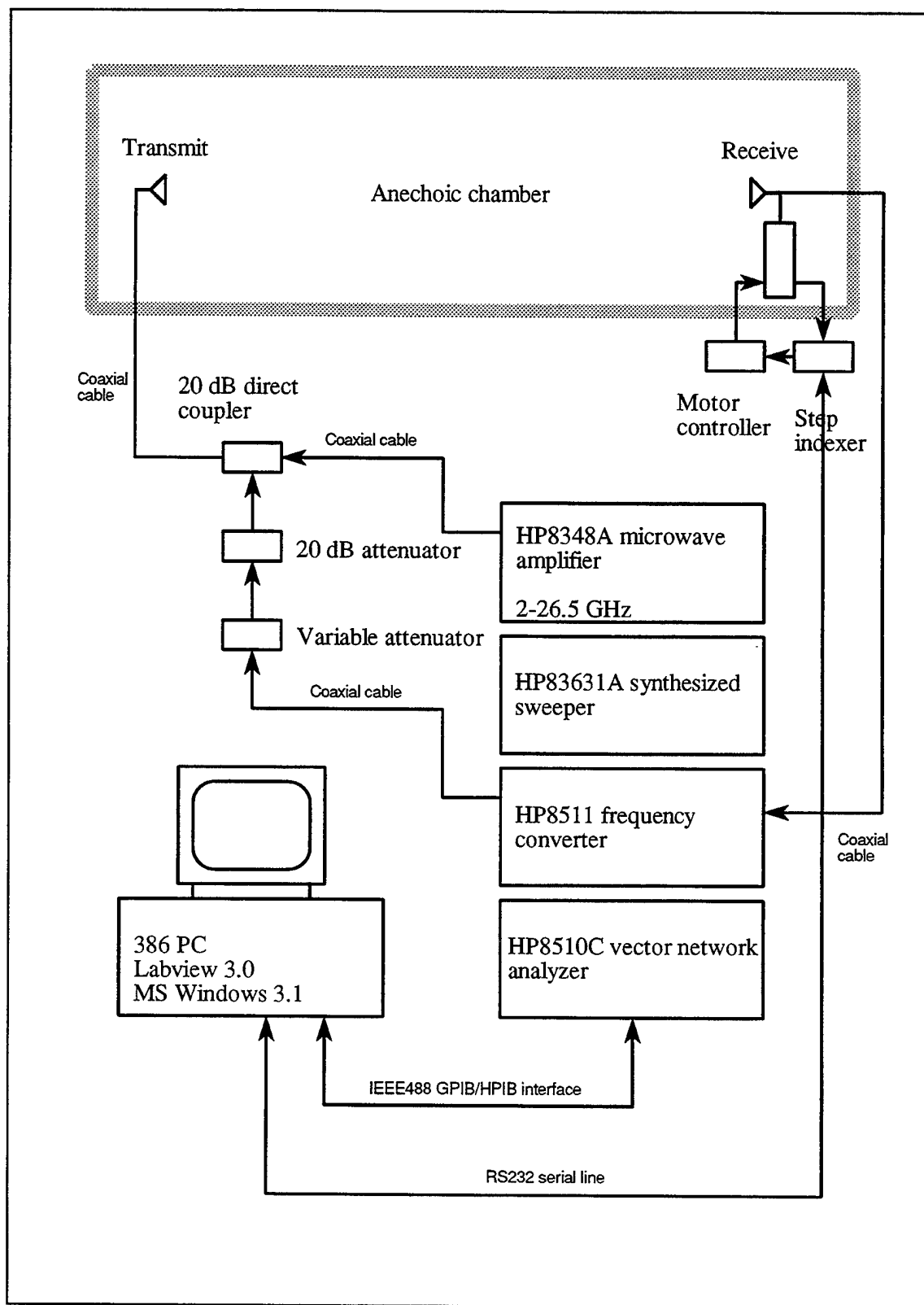


**Figure 4.2** Anechoic chamber facility

H-planes of the exponentially tapered 56X1 horn. Phase centers were then obtained for the horn using the graph in [Ref. 9]. Using these estimates, the antenna model used in PATCH was offset from the physical aperture plane (i.e., the location of the horn aperture when measurements were made) by the phase center distance. This adjustment is shown in Figure 4.3.

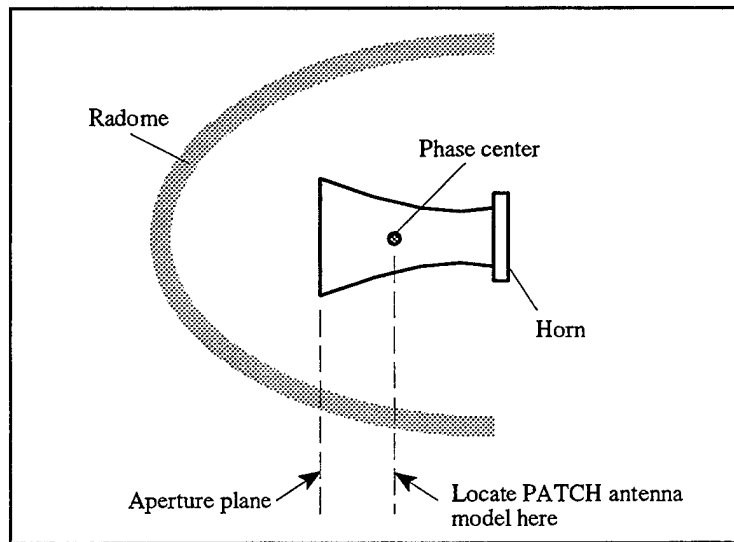


**Figure 4.3** Phase center adjustment

The E- and H-plane phase centers are an approximation since the 56X1 horn is not a true sectoral horn in either plane. To obtain the best phase center location, the PATCH antenna model was stepped through different locations about the initial estimate until the calculated antenna patterns converged to the measured patterns. This location was then deemed the phase center for a given plane. The final values for the 56X1 antenna are 0.0 cm for the E-plane and -3.0 cm for the H-plane. In other words, the E-plane phase center is coincident with the horn aperture, while the H-plane phase center lies 3.0 cm behind it.

### C. AGM-88 HARM RADOME

Pattern measurements were made on an AGM-88 High Speed Antiradiation Missile (HARM) radome that was mounted on the chamber pedestal in front of the Microline 56X1 antenna. This set up is shown in the upper part of Figure 4.4. The position of the antenna's aperture plane relative to the radome was noted so that an adjustment to the horn's phase center could be made in the computer model.

A computer model for the HARM/56X1 antenna configuration mentioned above was generated, and is shown in Figure 4.5. The antenna model was located at the E- or H-plane phase center for each respective pattern calculation.

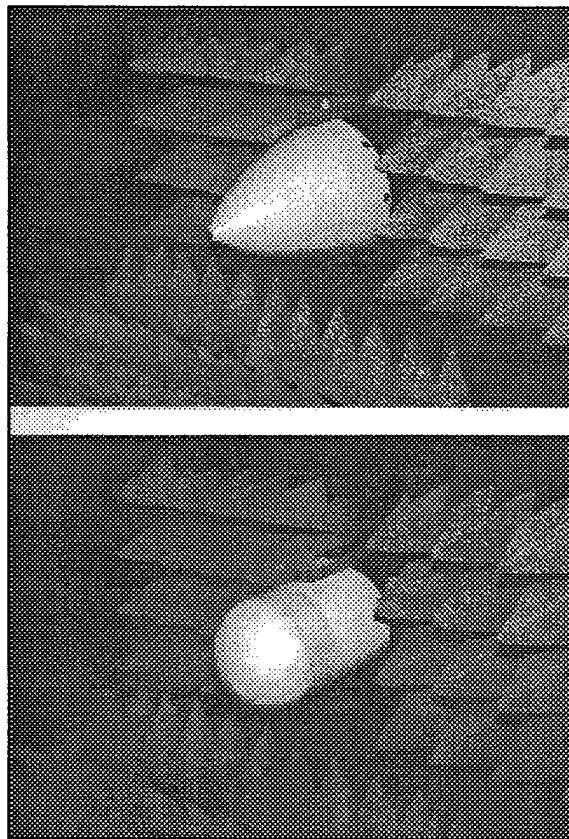


**Figure 4.4** HARM (upper) and AIM-9C (lower) radomes in anechoic chamber

Before a comparison of calculated results with measured data can be made, it is important to examine the effects of both radome and aperture impedance on the computer generated results. First, the effect of varying aperture impedance was examined. This is the impedance of the rectangular aperture plate that was used as the model for the Microline 56X1 antenna. Figure 4.6 shows the E- and H-plane patterns for aperture impedances of 100, 500, and 10,000 ohms. The E-plane pattern shows the most change. As impedance is increased, the side lobe peaks tend to migrate toward the center ( $\theta = 0^\circ$ ) and the main beam narrows approximately  $5^\circ$  at -10 dB. Side lobe levels in the E-plane are decreased with increasing aperture impedance. The H-plane pattern shows relatively little change with increasing aperture impedance. The main beam shows virtually no change, and side lobe levels are not significantly affected. There is some movement toward the center (as in the

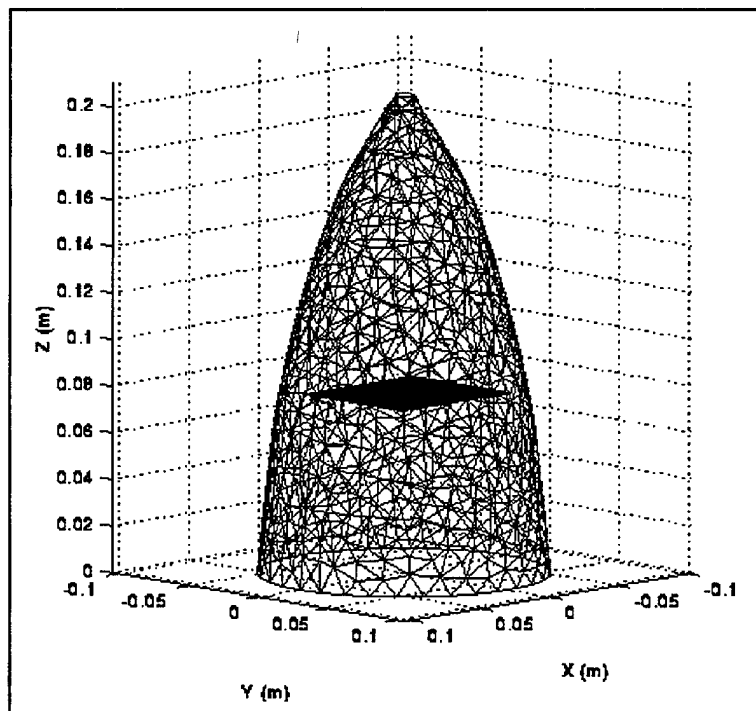


Figure 4.5 HARM radome model

E-plane) in the second and third side lobes. Thus, the value of aperture impedance determines how transparent the antenna is to waves reflected and scattered back from the radome. Figure 4.6 shows that the effect of aperture impedance on the HARM/56X1 model is minimal. There are no gross pattern changes. The effects are mainly in the low side lobe levels and in azimuth.

Secondly, the effect on radome impedance was examined. The surface impedance for the HARM radome is  $278-j31$  ohms, as calculated in Chapter III. Pattern calculations were made with two additional values of radome impedance,  $208-j41$  ohms and  $365-j54$  ohms. The effects of varying this impedance are shown in Figure 4.7. In both E- and H- planes the main beam is virtually not affected and there is a slight decrease in side lobe level with increasing radome impedance. This indicates that the more transparent the radome is (i.e., the greater the impedance) the less the magnitude of reflections between the antenna and radome. Overall, the effect of radome impedance in the HARM/56X1 model is minimal, with only low side lobe levels being affected.

Now that the effects of radome and aperture impedance have been examined, a comparison to measured data can be made. The values of radome and aperture impedance used in PATCH were  $278-j31$  ohms and 100 ohms, respectively. These values gave the best agreement with measured data. The patterns are shown in Figure 4.8. The E-plane patterns show the same general agreement in side lobe structure although the measured side lobes are 3-5 dB higher. The main beam patterns agree well down to -7 dB where the

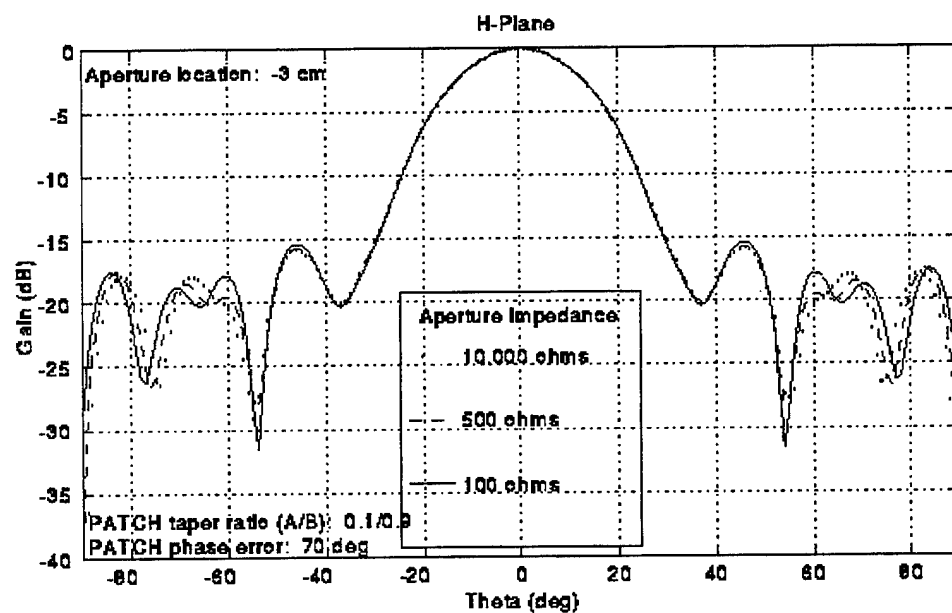
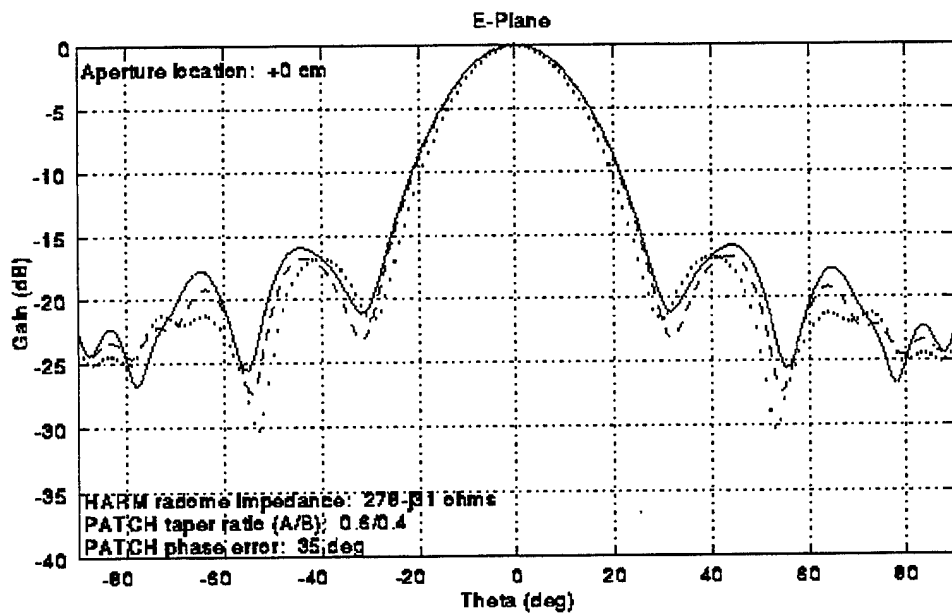


Figure 4.6 Effect of varying aperture impedance

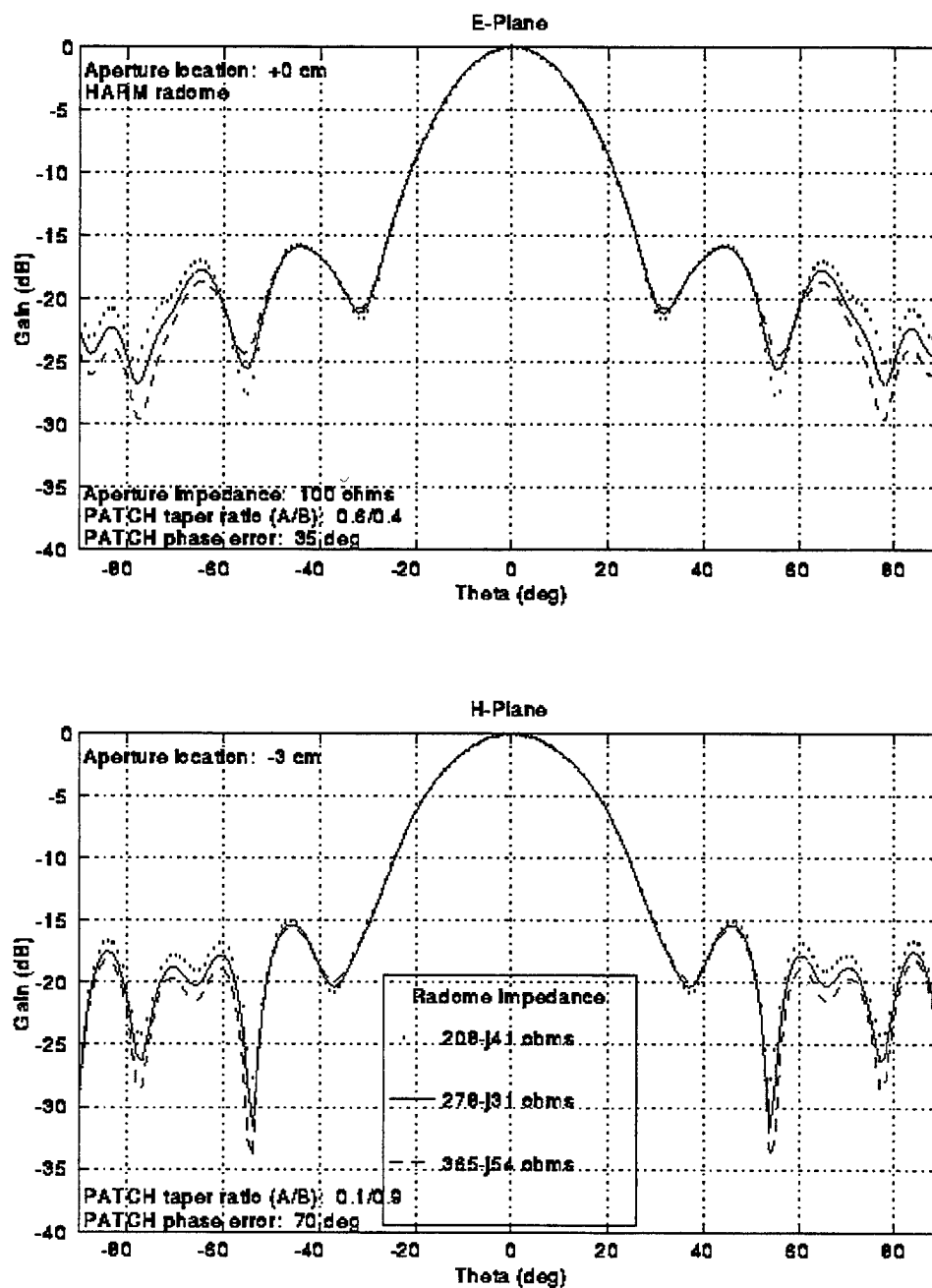


Figure 4.7 Effect of varying radome impedance



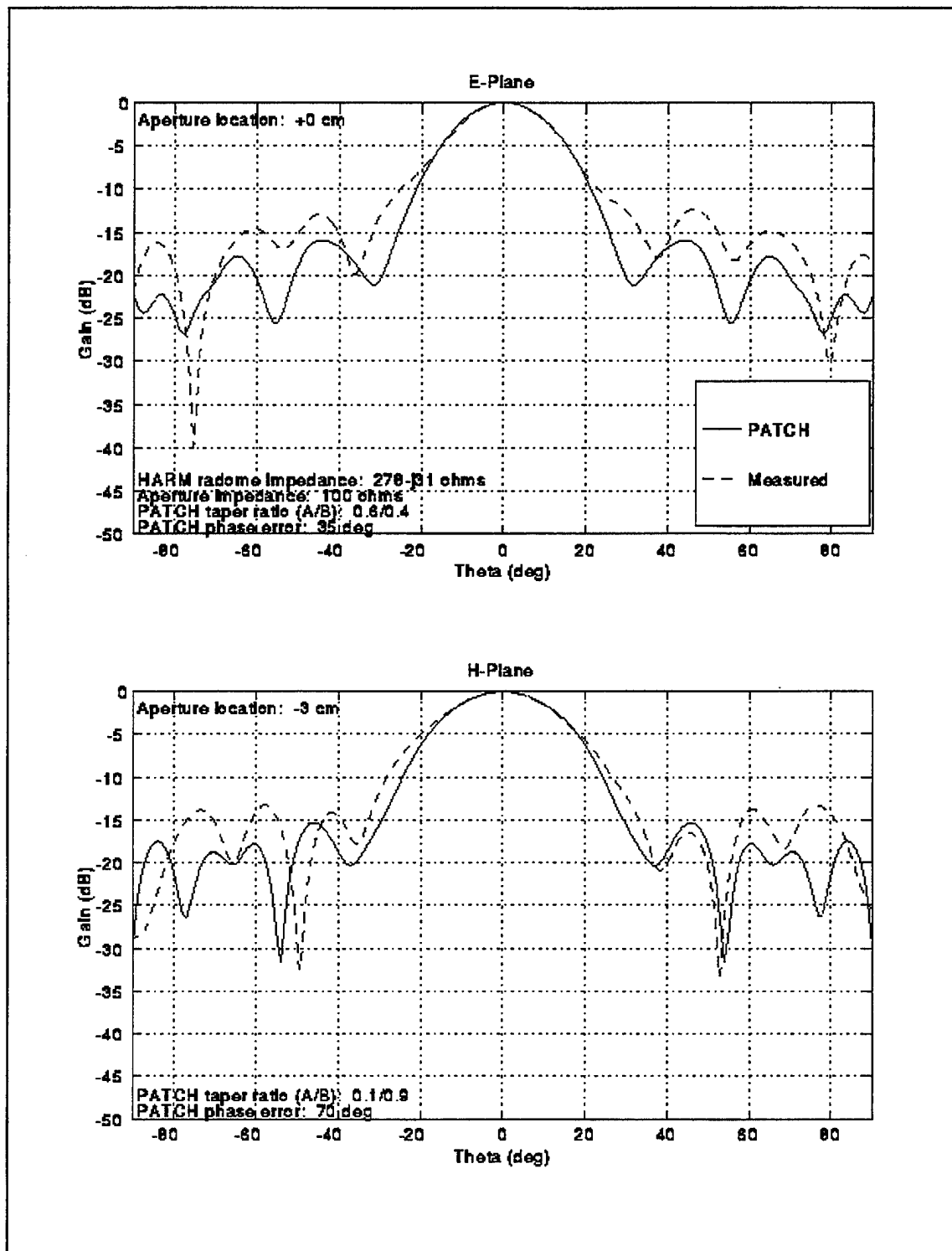


Figure 4.8 Comparison of measured and computed patterns for HARM radome

measured beam broadens by approximately  $6^\circ$ . This is characteristic of a large quadratic phase error or surface wave and will be addressed further in Chapter V. The H-plane pattern shows good agreement in the side lobe structure, and better agreement than the E-plane pattern in the main beam region.

#### **D. AIM-9C RADOME**

Pattern measurements were also made on an AIM-9C radome mounted on the chamber pedestal in front of the Microline 56X1 antenna. The position of the antenna's aperture plane relative to the radome was noted so that an adjustment to the horn's phase center could be made in the computer model.

The PATCH computer model of the AIM-9C/56X1 antenna configuration is shown in Figure 4.9. The actual radome and antenna as mounted on the chamber pedestal is shown in the lower part of Figure 4.4. The antenna model was located at the E- or H-plane phase center for each respective pattern calculation.

As with of the HARM radome, the effects of aperture and radome impedance were examined for the AIM-9C radome and 56X1 model. Figure 4.10 shows the effect of varying aperture impedance. In the E-plane, increasing impedance narrows the main beam and alters the side lobe pattern. In the H-plane the main beam is largely unchanged while the side lobe structure is markedly changed. This was a key factor in determining the best choice for aperture impedance. A value of 100 ohms produced the best agreement with measured data.

The effect of radome impedance is shown in Figure 4.11. Both E- and H-plane patterns show only minimal changes as the impedance is varied above and below the value of  $234-j166$  ohms that was determined in Chapter III. This minimal effect is most likely the

result of the AIM-9C radome being spherical in shape. Most of the reflected waves between the aperture and radome are at normal incidence to the radome.

For the comparison of measured and calculated patterns, an aperture impedance of 100 ohms was used. This is the same value used for the HARM radome case. The radome impedance was  $234-j166$  ohms. Both of these values produced results that matched the characteristics of the measured patterns. The comparison is shown in Figure 4.12. The E-plane patterns have the same basic shape, yet the measured side lobes are approximately 5 dB higher. There is good agreement in the main beams of the H-plane pattern, but some variation between the side lobe patterns.

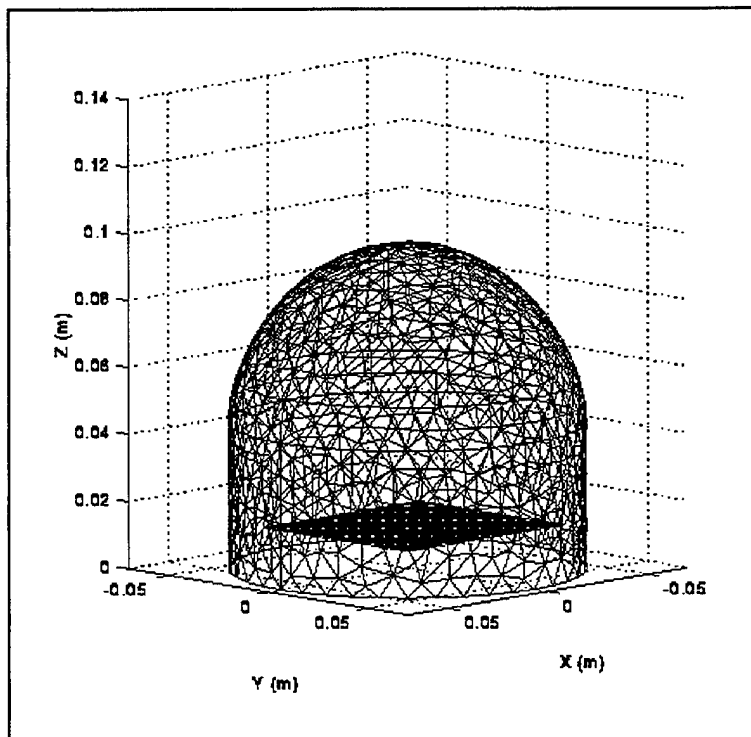


**Figure 4.9** AIM-9C radome model

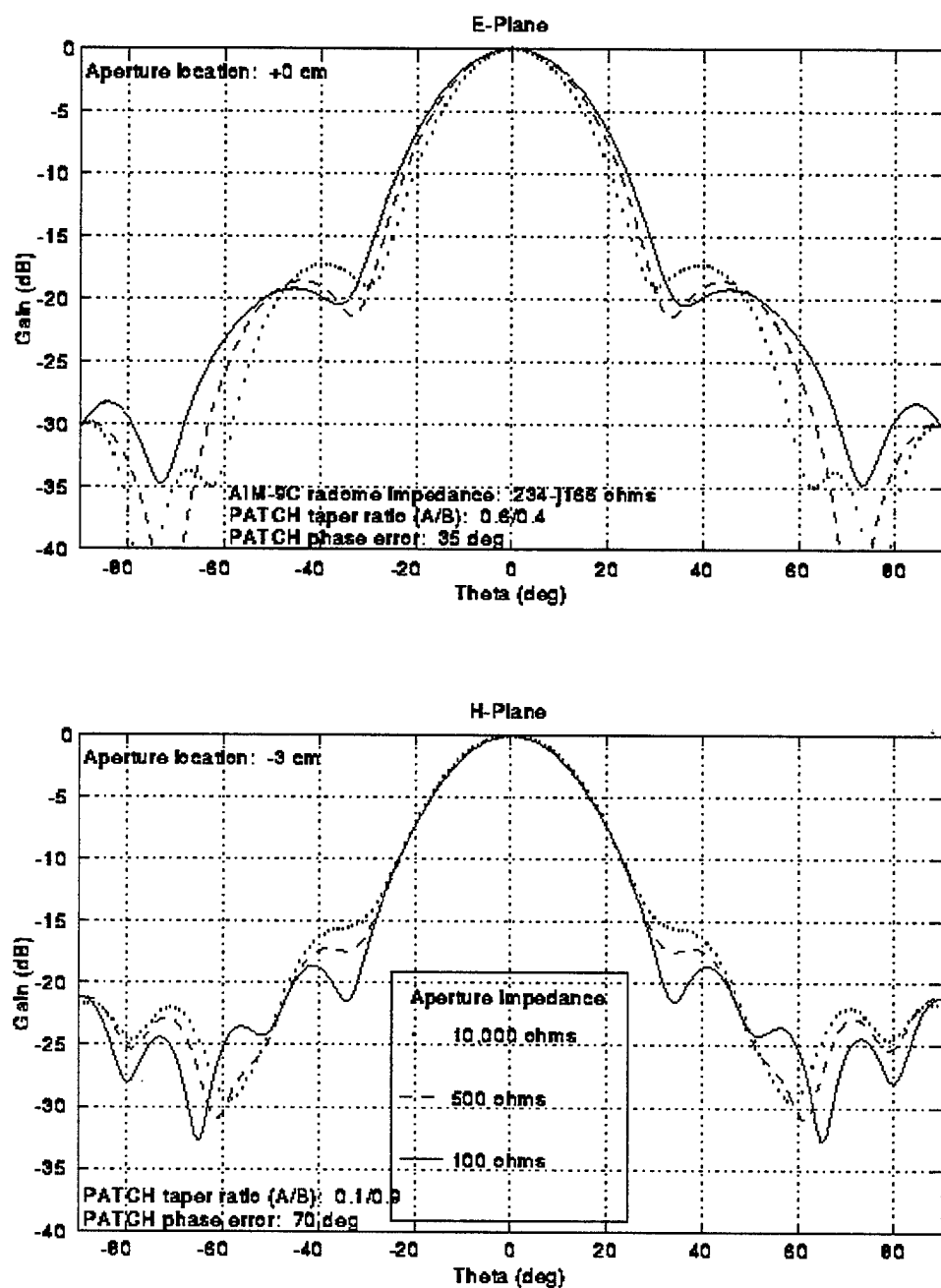


Figure 4.10 Effect of varying aperture impedance

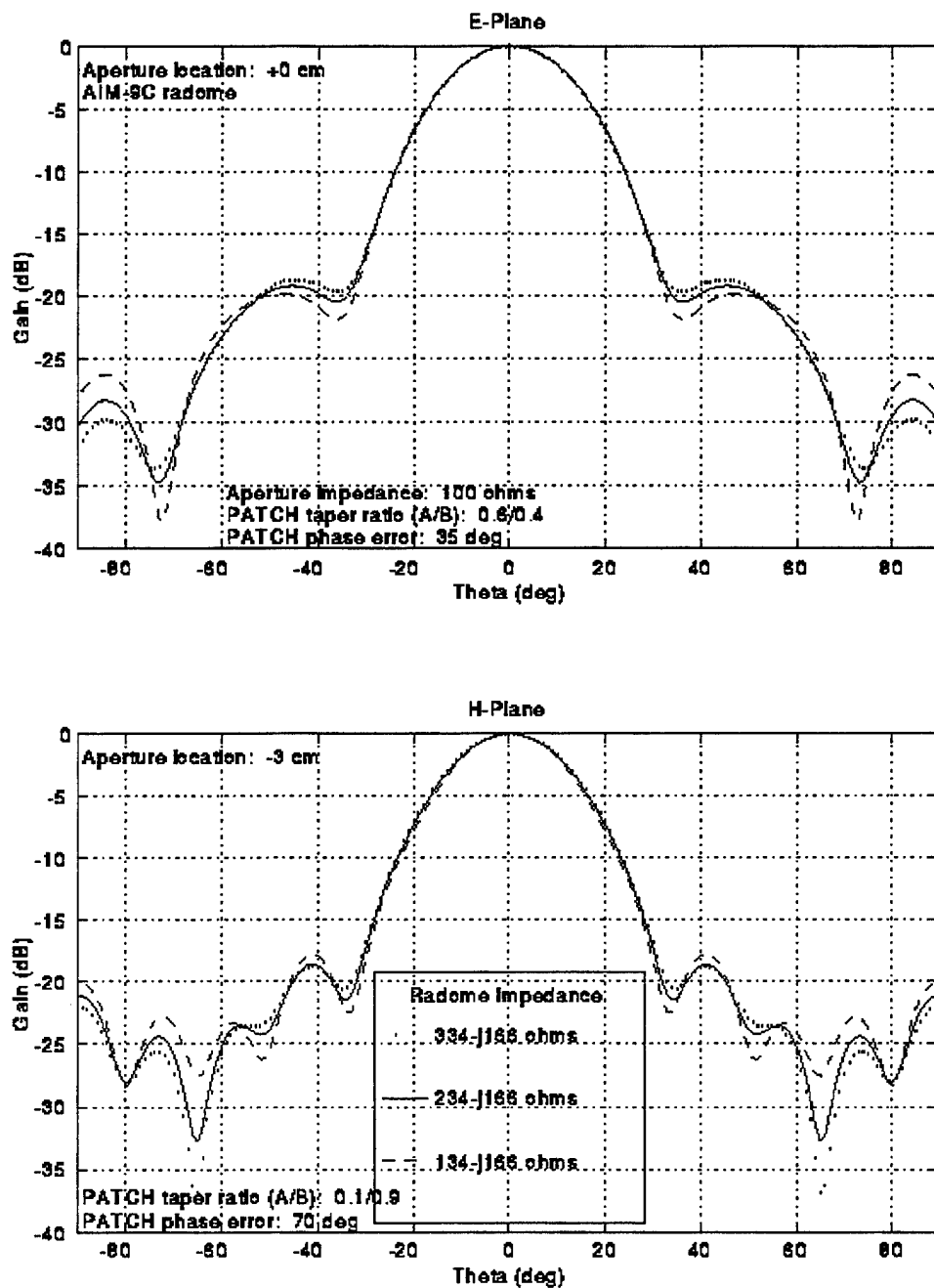
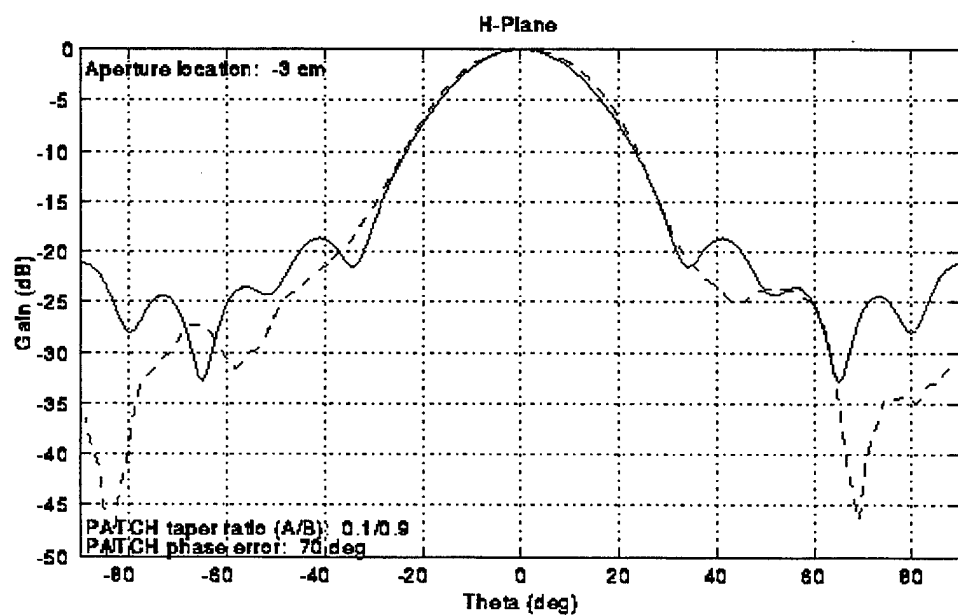
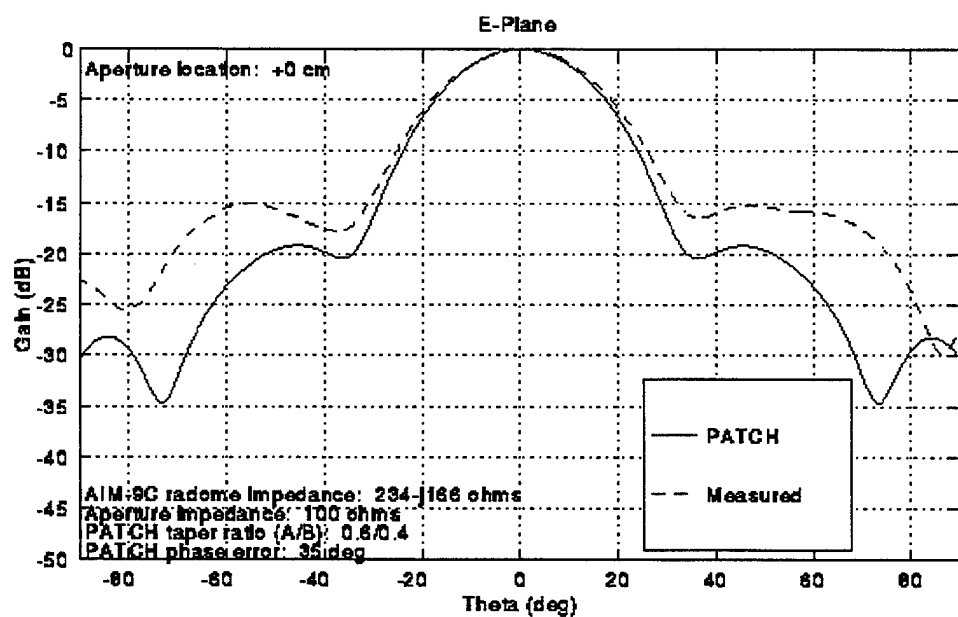


Figure 4.11 Effect of varying radome impedance



**Figure 4.12** Comparison of measured and calculated patterns for AIM-9C radome



## V. CONCLUSION

The analysis of radomes presented in this thesis uses a method of moments (MM) solution to the electric field integral equation. The method of moments provides a rigorous solution that is well-suited for computer coding. The MM computer codes available at the Naval Postgraduate School are RADOME and PATCH. The primary objective of this study was to evaluate PATCH, since it provides a higher degree of flexibility and accuracy than RADOME. The collection of pre- and post-processing programs that support PATCH is described in Chapter II. That chapter serves as a condensed "user's manual" for PATCH that provides sufficient details for modeling antenna and radome problems.

The PATCH code antenna model was validated in Chapter III by comparing the computed patterns to measured data. Once validated, PATCH was shown to be more versatile than RADOME in a number of areas. First, PATCH can model any arbitrary radome shape, while RADOME is limited to bodies of revolution. Second, PATCH takes into account all multiple reflections between the radome and antenna. The calculation of this interaction is desirable for predicting radome performance at wide angles ( $\theta \rightarrow 90^\circ$ ).

The analysis of the HARM and AIM-9C radomes demonstrate the versatility of PATCH. Models were developed for the antenna aperture and radomes, and a range of materials (impedances) were examined. Comparisons of the calculated patterns with measured ones yielded good agreement. The pattern differences of approximately 2-5 dB are mainly in the side lobes. The results of the analysis with PATCH strongly suggests that



fundamentals of accurate computer modeling exist. However, further refinements can still be made.

There are several possible sources of error in both the computer model and the anechoic chamber measurements. Computer model errors include: (1) approximate surface impedance of the radome, (2) inaccurate modeling of the radome base and rim, and (3) inaccurate antenna modeling. The HARM and AIM-9C radome models assume an average surface impedance over the entire radome. In practice, waves from the antenna will have different incidence angles along the surface of the radome. Since surface impedance is a function of incidence angle, the impedance should vary along the surface as well. A more accurate model of the radomes would include this impedance variation as a function of position on the radome. It is expected that this would induce focusing of the main beam and alter the side lobe pattern.

The HARM radome has a hard plastic ring which was not included in the antenna model. The AIM-9C radome model could be further improved by including the metal cylinder that is attached to the dielectric radome shell. This cylinder, or ring, is bonded to the base of the alumina shell and serves as a means of attachment to the missile body. It was not removable, and thus the entire assembly was mounted in the chamber (see Figure 4.4). Although the cylinder was behind the antenna aperture and out of the field of view out to  $\theta = 90^\circ$ , back scattering from this piece could influence pattern measurements. A more accurate computer model would include this cylinder.

The antenna aperture model (Figure 3.2) attempts to simulate the Microline 56X1 antenna as closely as possible. The aperture illumination is tapered, with quadratic phase error introduced, and the aperture plane is displaced to the phase center. Despite these adjustments, some minor discrepancies remain when comparing the antenna pattern radiated in free space to measured data. One possible source of the differences is edge diffraction.

Insofar as measurements are concerned, sources of error include: (1) radome mounts, and (2) imperfections in the anechoic chamber. The hardware that is used to mount the radomes in front of the 56X1 antenna can introduce additional scattering. The radomes are supported by two braces made of phenolic material. Although precautions were taken to ensure the radomes were centered in front of the antenna, some sagging or misalignment could have occurred, which results in pattern asymmetries.

Ideally, an anechoic chamber simulates free space by absorbing all waves incident on its walls. In practice, the walls will scatter and reflect some of the incident waves, especially if the absorbent material has been damaged or is deteriorated. The shape of the chamber also plays a role in measurement error. The Naval Postgraduate School's chamber has as a slanted corner wall which makes it asymmetrical with respect to the chamber's centerline. If radiation were to be scattered from this wall, pattern asymmetries would arise. The asymmetrical nature (with respect to  $\theta = 0^\circ$ ) of the measured patterns is partially due to the chamber's slanted corner wall.

A characteristic of composite radomes is that they are mildly anisotropic. The dielectric constant is polarization dependent because of the sandwich construction. For example, the HARM radome, which is a fiberglass composite sandwich, has a slightly

different pattern for a cut measured at the 12 o'clock position than it would at the 3 o'clock position. Although the HARM is as a symmetric body of revolution, very small discontinuities in the composite material can lead to noticeable pattern variations as the radome is rotated about the longitudinal axis [Ref. 10]. The same characteristics have been observed on the AIM-9C radome.

Figures 5.1 and 5.2 show the effect of placing a radome in front of an antenna aperture. Figure 5.1 shows the effect with the HARM radome, and Figure 5.2 shows the effect with the AIM-9C radome. All of the plots are calculated patterns from PATCH. In both cases, the main beam is largely unchanged, while the side lobe pattern and levels are altered significantly.

This thesis has established that PATCH is a powerful radome analysis tool. PATCH is highly versatile and can accommodate any radome shape or configuration, with size limited only by available computer memory. Its accuracy is mainly limited to the fidelity of the antenna and radome models. Future work should concentrate on determining the level of model detail that is required for a specified pattern level accuracy. This will require accurate surface impedance and antenna models. In the case of antenna scanning the surface impedance will change because the angle of incidence on the radome changes. Finally, the gain with and without the radome should be computed. In general this requires numerical integration of the field scattered by the radome.

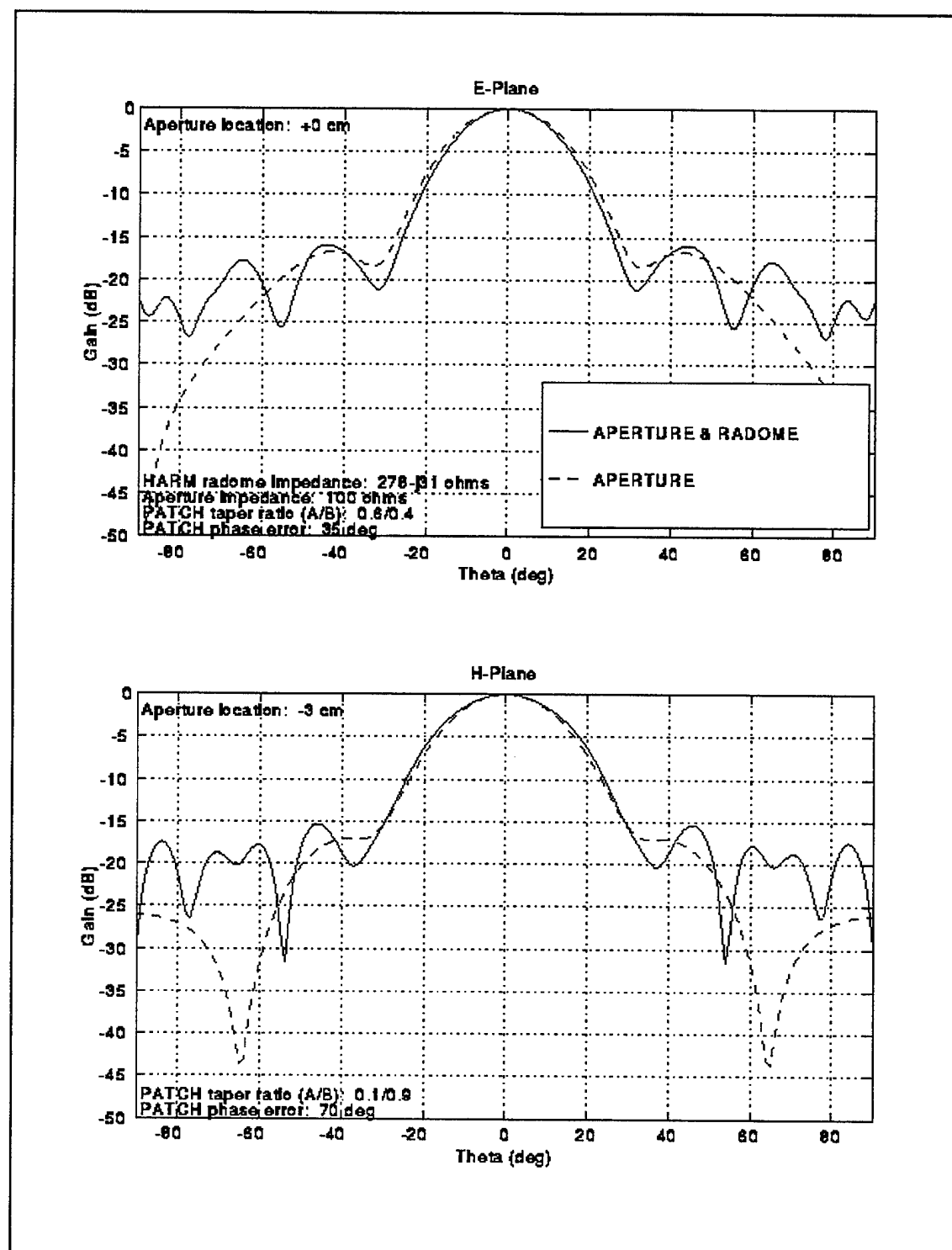


Figure 5.1 Effect of HARM radome on antenna pattern

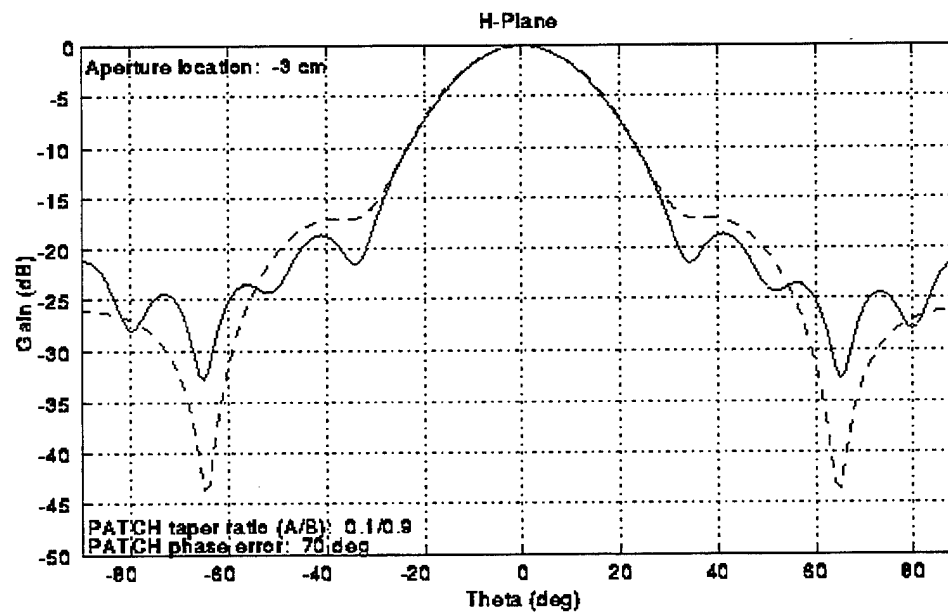
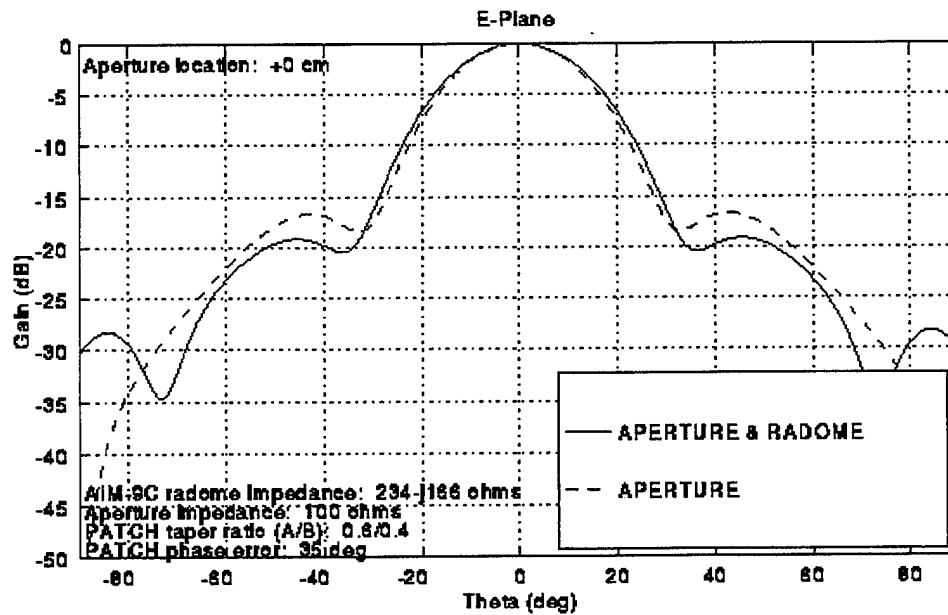


Figure 5.2 Effect of AIM-9C radome on antenna pattern

## APPENDIX A. PROGRAM LISTING FOR IMPEDANCE CALCULATION

This appendix contains a listing of a MATLAB program that calculates the transformed free space impedance through a three-layered radome wall at various incidence angles. The real and imaginary impedance values are plotted versus incidence angle.

```
clear
% Programmers: Prof. D.C. Jenn, various.
% compute equivalent radome surface impedance
%tincd=input('enter incidence angle (deg)');
%tinc=tincd*pi/180;
f=10.;
start=0.;
stop=80.;
dth=1.;
N=round((stop-start)/dth)+1;
w=3e8/f/1e9;
for m=1:N
    tincd=start+dth*(m-1);
    tinc=tincd*pi/180.;
% thickness of each region
d1=.100*.0254/cos(tinc);
d2=.15*.0254/cos(tinc);
d3=.05*.0254/cos(tinc);
% relative dielectric constants
er1=3.5;
er2=1.5;
er3=3.5;
k=2*pi/w;
% assume lossless radome materials (alpha1=alpha2=alpha3=0). Find betas.
a1=0.;
a2=0.;
a3=0.;
b1=k*sqrt(er1);
b2=k*sqrt(er2);
b3=k*sqrt(er3);
g1=a1+j*b1;
g2=a2+j*b2;
g3=a3+j*b3;
% characteristic impedance of each section
z0=377./cos(tinc);
z1=z0*sqrt(1./er1);    % assumes theta_i in each region
z2=z0*sqrt(1./er2);
z3=z0*sqrt(1./er3);
% impedances looking into each boundadry
zc=z3*(z0+z3*tanh(g3*d3))/(z3+z0*tanh(g3*d3));
zb=z2*(zc+z2*tanh(g2*d2))/(z2+zc*tanh(g2*d2));
za=z1*(zb+z1*tanh(g1*d1))/(z1+zb*tanh(g1*d1));
% reflection coefficient at the input
%R(m)=((za-z0)/(za+z0));
```

```

T(m)=tincd;
Re(m)=abs(za);
Im(m)=atan2(imag(za),real(za))*180/pi;
end
subplot(211),plot(T,Re),grid
xlabel('ANGLE OF INCIDENCE (DEG)')
ylabel('MAGNITUDE (OHMS)')
subplot(212),plot(T,Im),grid
xlabel('ANGLE OF INCIDENCE (DEG)')
ylabel('PHASE (DEG)')

```

## APPENDIX B. SAMPLE INPATCH FILE LISTING

The appendix contains a listing of the file *inpatch* for the quadrangle shown in Figure 2.8. There are 20 edges and 43 nodes. The nodes are listed first, with their respective Cartesian coordinates ( $x, y, z$ ). The edge segments are listed next, with their respective endpoint nodes.

The last block of data defines the calculation parameters. For this case there are two voltage potentials (between nodes 4 and 5 and nodes 7 and 8), each with a value of  $1.2 + j0.9$  volts. There are two surface impedance faces (11 and 12), with a value of  $100 + j200$  ohms. Calculations are specified for  $0^\circ \leq \theta \leq 90^\circ$  at  $1^\circ$  increments. The observation plane is  $\phi = 90^\circ$  and the frequency 10 Ghz.

sample inpatch file, comment line

20	43			
1		0.000000E+00	0.000000E+00	0.000000E+00
2		0.000000E+00	1.000000E+00	0.000000E+00
3		0.000000E+00	2.000000E+00	0.000000E+00
4		0.000000E+00	3.000000E+00	0.000000E+00
5		1.000000E+00	0.000000E+00	0.000000E+00
6		1.000000E+00	1.000000E+00	0.000000E+00
7		1.000000E+00	2.000000E+00	0.000000E+00
8		1.000000E+00	3.000000E+00	0.000000E+00
9		2.000000E+00	0.000000E+00	0.000000E+00
10		2.000000E+00	1.000000E+00	0.000000E+00
11		2.000000E+00	2.000000E+00	0.000000E+00
12		2.000000E+00	3.000000E+00	0.000000E+00
13		3.000000E+00	0.000000E+00	0.000000E+00
14		3.000000E+00	1.000000E+00	0.000000E+00
15		3.000000E+00	2.000000E+00	0.000000E+00
16		3.000000E+00	3.000000E+00	0.000000E+00
17		4.000000E+00	0.000000E+00	0.000000E+00
18		4.000000E+00	1.000000E+00	0.000000E+00
19		4.000000E+00	2.000000E+00	0.000000E+00
20		4.000000E+00	3.000000E+00	0.000000E+00



```

1      1      2
2      2      3
3      3      4
4      1      5
5      1      6
6      2      6
7      2      7
8      3      7
9      3      8
10     4      8
11     5      6
12     6      7
13     7      8
14     5      9
15     5     10
16     6     10
17     6     11
18     7     11
19     7     12
20     8     12
21     9     10
22    10     11
23    11     12
24     9     13
25     9     14
26    10     14
27    10     15
28    11     15
29    11     16
30    12     16
31    13     14
32    14     15
33    15     16
34    13     17
35    13     18
36    14     18
37    14     19
38    15     19
39    15     20
40    16     20
41    17     18
42    18     19
43    19     20
0
0  0  0
1
v
2
4      5  1.20000E+00  0.90000E+00
7      8  1.20000E+00  0.90000E+00
0
2
11     1.00000E+02  2.00000E+02
12     1.00000E+02  2.00000E+02
.false.  0  0
1
0.    90.0000  91    90.0000  90.0000  1
0

```

```
.false.  
0  
  1.00000E+10  
-1.00000
```



## APPENDIX C. PROGRAM LISTING FOR VOLTAGE TAPERING

This appendix contains a listing of a MATLAB program that calculates a two-dimensional array of voltage excitations across a rectangular grid. The voltages are tapered, with a cosine on a pedestal distribution. The voltages are at the pedestal value at the edge of the grid, and highest (1 volt) at the center.

The variables that are defined at the beginning of the program specify the grid size and distance between individual voltage slits. The maximum quadratic phase error at the edge of the grid is specified by *px* and *py*. The parameters that specify the cosine on a pedestal taper are in *tapx* and *tapy*.

```
%
% Program name: TAPER.M
% Programmer: LT Scott M. Herzog, USN
% January 1996
%
% Program for indexing segments, nodes, and voltages
% for use in INPATCH.

clear
a= 0.078;           % width of waveguide (meters)
xl= -0.030;         % x-coord. of center of first segment
dx= 0.012;          % increment between segments
xn= 0.030;          % x-coord. of center of last segment
b= 0.066;           % height of waveguide (meters)
yl= 0.033;          % y-coord. of first row
dy= -0.006;         % increment between rows
yn= -0.033;         % y-coord. of last row
seg1= 42;           % number of 1st segment in block
dseg= 2;            % increment between segments
segn= 52;           % number of last segment in block
jseg= 30;           % jump in segment increment (last to first)
jlseg=40;           % jump from last to last segment
nod1= 2;            % number of 1st node in block
dnod= 2;            % increment between nodes
nodn= 12;           % number of last node in block
jnod= 4;            % jump in node increment (last to first)
jlnod=14;           % jump from last to last node
px= 70;             % phase error in x-dir (deg), H-plane
py= 35;             % phase error in y-dir (deg), E-plane
n=0;
for y=y1:dy:yn;
```

```

        for x=x1:dx:xn;
            n=n+1;
            phx=exp(j*px*pi/180*(2*x/a)^2);
            phy=exp(j*py*pi/180*(2*y/b)^2);
            tapx=(0.1+0.9*cos(pi*x/a)); % H-plane taper
            tapy=(0.6+0.4*cos(pi*y/b)); % E-plane taper
            v=tapx*tapy*phx*phy;
            volt(n)=v;
        end
    end
end
n=0;
for y=y1:dy:yn;
    for seg=seg1:dseg:segn;
        n=n+1;
        segment(n)=seg;
    end
    seg1=segn+jseg;
    segn=segn+jlseg;
end
n=0;
for y=y1:dy:yn;
    for nod=nod1:dnod:nodn;
        n=n+1;
        node(n)=nod;
    end
    nod1=nodn+jnod;
    nodn=nodn+jlnod;
end
data=[segment' node' real(volt)' imag(volt)'];
save volt n data -ascii

```

## APPENDIX D. PROGRAM LISTING FOR GEOMETRY COMBINING

This appendix contains a listing of a MATLAB program to combine two separate elements of geometry, such as an aperture and a radome. If the aperture geometry was created separately from the radome geometry, each file's nodes and edges are numbered independently, starting with the number one. A geometry file cannot be appended to another, until the second file's nodes and edges are renumbered. This program renumbers the nodes and edges of the second geometry file, appends it to the first, and saves the combined file under the name *duo*.

```
% Program name:    COMBINE.M
% Programmer:      LT Scott M. Herzog, USN
% April 1996
%
% Combines two independent ASCII data files from the output of
% BUILDN5.X.
%
% Re-indexes the node and edge numbers of the second data file
% and appends it to the first.
%
% Notes on usage:
%
% (1) Delete comment line in both input files.
% (2) Rename first input file FILE1.TXT, typically the aperture.
% (3) Rename second input file FILE2.TXT, typically the radome.
% (4) Output file saved as DUO, without a comment line.
%     This must be added!

clear
id1 = fopen('file1.txt','rt');      % read in first file.
file1= fscanf(id1,'%e');
id2 = fopen('file2.txt','rt');      % read in second file.
file2= fscanf(id2,'%e');

nodes1 = file1(1,1);
edges1 = file1(2,1);
nodes2 = file2(1,1);
edges2 = file2(2,1);

an1 = 3;          % row no. of first element in node block in file1.
zn1 = nodes1*4+2; % " " " last " " " " " " " "
ae1 = zn1+1;      % row no. of first element in edge block in file1.
ze1 = zn1+edges1*3; % " " " last " " " " " " " "
an2 = 3;
```

```

zn2 = nodes2*4+2;
ae2 = zn2+1;
ze2 = zn2+edges2*3;

comb=[nodes1+nodes2 edges1+edges2];

N1=reshape(file1(an1:zn1,1),4,nodes1);    % construct node block matrix
N1=N1';
E1=reshape(file1(ae1:ze1,1),3,edges1);    % construct edge block matrix
E1=E1';
N2=reshape(file2(an2:zn2,1),4,nodes2);
N2=N2';

N1(:,4) = N1(:,4) + 0.07699;              % translate aperture forward.

N2(:,4) = N2(:,4) - 0.1452;              % subtract offset in Z-axis.
%N2(:,2:4) = 0.001*N2(:,2:4);            % rescale from mm to m.
%N2(:,2:4) = 0.0254*N2(:,2:4);           % rescale from in to m.
%N2(:,2:4) = 0.0205*N2(:,2:4);           % rescale from 'units' to m.
N2(:,2:4) = 0.0282369*N2(:,2:4);         % rescale to m, for some files.

E2=reshape(file2(ae2:ze2,1),3,edges2);
E2=E2';

N2(:,1)=N2(:,1)+nodes1;                  % changes node numbers in second file.
E2(:,1)=E2(:,1)+edges1;                  % changes edge numbers in second file.
E2(:,2:3)=E2(:,2:3)+nodes1;

save duo comb N1 N2 E1 E2 -ascii

```

## LIST OF REFERENCES

1. Jenn, D. C., Radar and Laser Cross Sectional Engineering, AIAA Education Series, June 19, 1995.
2. Francis, R. M., "A Computer Model for the Transmission Characteristics of Dielectric Radomes," Master's Thesis, Naval Postgraduate School, Monterey, California, March 1992.
3. Klopp, K. A., "Antenna Gain Loss and Pattern Degradation due to Transmission Through Dielectric Radomes," Master's Thesis, Naval Postgraduate School, Monterey, California, March 1993.
4. Johnson, W. A., Wilton, D. R., and Sharpe, R. M., Patch Code Users' Manual, Sandia Report SAND87-2991, May 1988.
5. Sadiku, M. N. O., Elements of Electromagnetics, second edition, Saunders College Publishing, 1994, p. 466.
6. Chang, D. C., "A Comparison of Computed and Measured Transmission Data for the AGM-88 HARM Radome," Master's Thesis, Naval Postgraduate School, Monterey, California, September 1993.
7. Jenn, D. C., Francis, R. M., and Klopp, K. A., "Computer Model for Axially Symmetric Dielectric Radomes in the Near Field of a Circular Aperture," unpublished notes, Naval Postgraduate School, Monterey, California.
8. Stutzman, W. L. and Thiele, G. A., Antenna Theory and Design, John Wiley & Sons, Inc., 1981, pp. 184-189.
9. Balanis, C. A., Antenna Theory Analysis and Design, John Wiley and Sons, Inc., 1982, pp. 587-589.
10. Hoppus, G. W., Radio Frequency Guidance Head, NAWCWPNS, China Lake, California, telephone conversation, May 1996.



